Article

Dexterous magnetic manipulation of conductive non-magnetic objects

https://doi.org/10.1038/s41586-021-03966-6

Received: 11 March 2021

Accepted: 26 August 2021

Published online: 20 October 2021

Check for updates

Lan N. Pham[1], Griffin F. Tabor[2], Ashkan Pourkand[2], Jacob L. B. Aman[3], Tucker Hermans[2,4] & Jake J. Abbott[1]✉

Dexterous magnetic manipulation of ferromagnetic objects is well established, with three to six degrees of freedom possible depending on object geometry[1]. There are objects for which non-contact dexterous manipulation is desirable that do not contain an appreciable amount of ferromagnetic material but do contain electrically conductive material. Time-varying magnetic fields generate eddy currents in conductive materials[2–4], with resulting forces and torques due to the interaction of the eddy currents with the magnetic field. This phenomenon has previously been used to induce drag to reduce the motion of objects as they pass through a static field[5–8], or to apply force on an object in a single direction using a dynamic field[9–11], but has not been used to perform the type of dexterous manipulation of conductive objects that has been demonstrated with ferromagnetic objects. Here we show that manipulation, with six degrees of freedom, of conductive objects is possible by using multiple rotating magnetic dipole fields. Using dimensional analysis[12], combined with multiphysics numerical simulations and experimental verification, we characterize the forces and torques generated on a conductive sphere in a rotating magnetic dipole field. With the resulting model, we perform dexterous manipulation in simulations and physical experiments.

Magnetic manipulation has the benefit of being contactless, which is particularly attractive when there is a risk of destructive collision between the manipulator and target. Such is the case with space debris[13,14], a considerable problem facing humanity owing to the Kessler syndrome[15]. Most artificial space objects are fabricated primarily from aluminium[16], a non-magnetic but conductive material on which forces and torques can be generated by inducing eddy currents. The most commonly proposed application of this phenomenon is detumbling satellites by applying a static magnetic field to a rotating target. There exist numerical solutions for induced forces and/or torques on spinning solid and thin-walled spheres in uniform and non-uniform magnetic fields[5–7]. An alternative method of detumbling satellites uses rotating Halbach arrays near the target[10]. Rotating Halbach arrays have also been proposed as a means of traversing the exterior of the International Space Station (modelled as an infinite flat plate) using forces induced by eddy currents[9]. This technique is similar to that used in eddy-current separation of non-magnetic materials[11]. Methods based on eddy currents are distinct from those based on diamagnetism[17] or ferrofluid environments[18], neither of which are applicable to manipulation of objects at a distance.

Here we show that dexterous manipulation of conductive objects is achievable using multiple static (in position) magnetic dipole-field sources capable of continuous dipole rotation about arbitrary axes. We demonstrate manipulation with six degrees of freedom (6-DOF manipulation) in numerical microgravity simulations and 3-DOF manipulation in experimental microgravity simulations. This manipulation does not rely on dynamic motion of the conductive object itself; rather, the manipulation can be performed quasistatically. Both electromagnet and permanent-magnet devices have been developed to serve as field sources capable of generating continuously rotating magnetic dipole fields about arbitrary axes[19,20]. Rotating magnetic dipole fields have been used previously to remotely actuate ferromagnetic devices that transduce the resulting magnetic torque into some form of rotational motion, such as micromachines and magnetic capsule endoscopes[1].

To make our problem tractable, we explicitly consider conductive spheres, which can serve as first-order approximations for other geometries. Furthermore, we characterize those spheres in three canonical positions relative to a rotating magnetic dipole, as depicted in Fig. 1. Using cylindrical coordinates, the z-axis aligns with the angular-velocity vector $\boldsymbol{\omega}$ of the rotating dipole, with the dipole always orthogonal to that vector. We consider positions in the $\pm z$ axial directions and the radial direction ρ. When using a magnetic dipole-field source capable of dipole rotation about arbitrary axes, any given position can be transformed into each of these canonical positions through the choice of the dipole rotation axis. The magnetic dipole can be abstracted as a point dipole $\mathbf{m}$ (units A m^2) at position $\mathcal{P}_{\mathbf{m}}$, which generates a magnetic field vector $\mathbf{b}$ (units T) at each position $\mathcal{P}_{\mathbf{b}}$ in space:

$$\mathbf{b}=\frac{\mu_0}{4\pi\|\mathbf{d}\|^3}\left(\frac{3\mathbf{d}\mathbf{d}^{\mathrm{T}}}{\|\mathbf{d}\|^2}-\boldsymbol{I}\right)\mathbf{m} \qquad (1)$$

[1]Department of Mechanical Engineering, University of Utah, Salt Lake City, UT, USA. [2]School of Computing, University of Utah, Salt Lake City, UT, USA. [3]Lawrence Livermore National Laboratory, Livermore, CA, USA. [4]NVIDIA, Seattle, WA, USA. ✉e-mail: jake.abbott@utah.edu

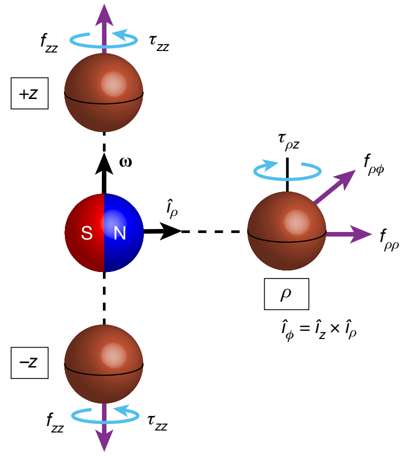

Fig. 1 | Induced forces and torques on a conductive sphere in three canonical positions relative to a rotating magnetic dipole. The dipole is spinning with angular velocity $\boldsymbol{\omega}$. Force and torque arrows are shown for all non-negligible components, with arrowheads depicting the actual directions corresponding to the $\boldsymbol{\omega}$ shown.

Table 1 | Induced force and torque, and the six independent parameters that affect them

Parameter		Units	Π group
Force induced on sphere	f	N	$\Pi_0 = fr^4\mu^{-1}m^{-2}$
Torque induced on sphere	τ	N m	$\Pi_0 = \tau r^3\mu^{-1}m^{-2}$
Sphere electrical conductivity	σ	$N^{-1}\,m^{-2}\,s\,A^2$	$\Pi_1 = \sigma\mu\omega r^2$
Distance from dipole to sphere	d	m	$\Pi_2 = dr^{-1}$
Sphere radius	r	m	
Dipole strength	m	$A\,m^2$	
Frequency of dipole rotation	ω	s^{-1} (Hz)	
Environment magnetic permeability	μ	$N\,A^{-2}$	

where $\mathbf{d} = \mathcal{P}_\mathbf{b} - \mathcal{P}_\mathbf{m}$ is the relative displacement vector (units m), I is the identity matrix, $\mu_0 = 4\pi \times 10^{-7}$ N A^{-2} is the permeability of free space, and all vectors are expressed in a common frame of reference[1].

We begin by characterizing the steady-state time-averaged forces and torques, in each of the canonical positions, as a function of the six independent variables enumerated in Table 1. These quantities collectively comprise four dimensions: N, m, s and A. The Buckingham Π theorem tells us that the underlying physics describing each of the two dependent variables, force and torque, can be characterized using just three dimensionless Π groups[12], with Π_0 expressed as a function of Π_1 and Π_2 (see Table 1 and Supplementary Information 1). The Buckingham Π theorem does not tell us anything about the form of these equations; that requires empirical characterization.

To derive functions that characterize eddy-current-induced forces and torques at $\pm z$ and ρ, we conducted electromagnetic finite-element-analysis (FEA) simulations using Ansys Maxwell software across a range of parameters (see Fig. 2a and Supplementary Information 2). It is from this FEA that we determined the non-negligible force and torque components shown in Fig. 1. We confirmed the expected symmetry of the $\pm z$ configurations, in which the force acts to push the sphere away from the rotating dipole, and the torque acts to rotate the sphere in the same direction as $\boldsymbol{\omega}$. At the ρ configuration, one component of the force pushes the sphere away from the rotating dipole, another component of the force pushes the sphere in the $\hat{i}_\phi = \hat{i}_z \times \hat{i}_\rho$ direction, and the torque acts to rotate the sphere opposite to $\boldsymbol{\omega}$.

When visualizing the resulting non-dimensional Π groups (see Fig. 2b and Supplementary Information 3), we observed that at relatively far distances ($\Pi_2 > 1.5$, approximately), the relationship between $\log_{10}(\Pi_0)$ and $\log_{10}(\Pi_2)$, for a given Π_1, is accurately described by a linear model, with a slope of −6 for torques and −7 for forces (these values are analogous to what is expected from magnetic torques and forces imparted by a magnetic dipole on a soft-magnetic object), and with an intercept that is a function of Π_1. The final unified model is of the form

$$\Pi_0 = \frac{(c_0\Pi_1)^{c_1\Pi_1^{c_2}}10^{c_3}}{\Pi_2^{c_4}} \tag{2}$$

The model coefficients c_1 to c_4, determined through least-squares regression, are provided for 'FEA' in Supplementary Table 2 of Supplementary Information 3. This model, although empirically determined, is well behaved in the sense that $\Pi_0 \to 0$ (that is, $f \to 0$ or $\tau \to 0$) as $\Pi_1 \to 0$ (for example, as $\omega \to 0$ or $\sigma \to 0$) or as $\Pi_2 \to \infty$ (for example, as $d \to \infty$), as expected from first principles. At relatively close distances, this model underpredicts the data, making the model conservative.

Next, we experimentally verified the model described above with an experimental set-up comprising a cubic NdFeB permanent magnet rotated by a direct-current (d.c.) motor, a solid copper sphere mounted on a 6-DOF force-torque sensor, and a 3D-printed pegboard that enables the copper sphere to be placed in the three configurations of interest (see Fig. 2c and Supplementary Information 4). A sample of the resulting data with regression models is presented in Fig. 2d. Using the complete experimental data set, we fit the model of equation 2, with the resulting coefficients provided under 'Experiments' in Supplementary Table 2 of Supplementary Information 3.

As we compare the experimental and FEA results across configurations and force-torque components, we find good agreement in the overall trends. The FEA-based model tends to overpredict the experimental values of Π_0 by a factor of 1.5–5.5. This discrepancy could be due to impurities in the copper sphere or from using a cubic permanent magnet. However, field distortions from a cubic magnet relative to a point-dipole model are typically less than 5% in our region of implementation[21]. It has also been previously noted that Ansys Maxwell tends to overpredict experimental results in similar situations[10]. Considering these factors, we suggest using the experiment-based model as a lower bound and the FEA-based model as an upper bound for Π_0. Extrapolating the model beyond the values of Π_1 and Π_2 considered should be done with caution.

We now describe a framework for using the force-torque model developed above to perform dexterous manipulation with magnetic-dipole sources surrounding the conductive object of interest. This can take the form of stationary or mobile permanent magnets or electromagnets. Here, we focus exclusively on the case of stationary electromagnets, in which both m and $\boldsymbol{\omega}$ can be controlled, but with their respective maximum values coupled due to the low-pass-filtering effect of induction. We treat m and the direction of $\boldsymbol{\omega}$ as the control variables and simply use a constant angular-velocity magnitude ω. We assume n electromagnetic dipole-field sources, with the ith source located at position $\mathcal{P}_{ei}$ and having an orientation described by a rotation matrix ${}^{W}R_{ei}$ with respect to some world frame[22]. We assume a single conductive object located at position $\mathcal{P}_c$ and having an orientation described by ${}^{W}R_c$ and a displacement vector $\mathbf{d}_i = \mathcal{P}_c - \mathcal{P}_{ei}$ with respect to each source.

To use the model in equation 2, we recast forces and torques in the forms $f = \Pi_0 r^{-4}\mu_0 m^2$ and $\tau = \Pi_0 r^{-3}\mu_0 m^2$, respectively. Each source is given a model frame, described by a relative rotation matrix ${}^{ei}R_{mi}$, defined such that its z-axis is parallel to $\mathbf{d}_i$. In the $\pm z$ configurations, $\boldsymbol{\omega}$ is parallel or antiparallel to the model-frame z-axis, and in the ρ configuration $\boldsymbol{\omega}$ is any vector orthogonal to the z-axis, with the

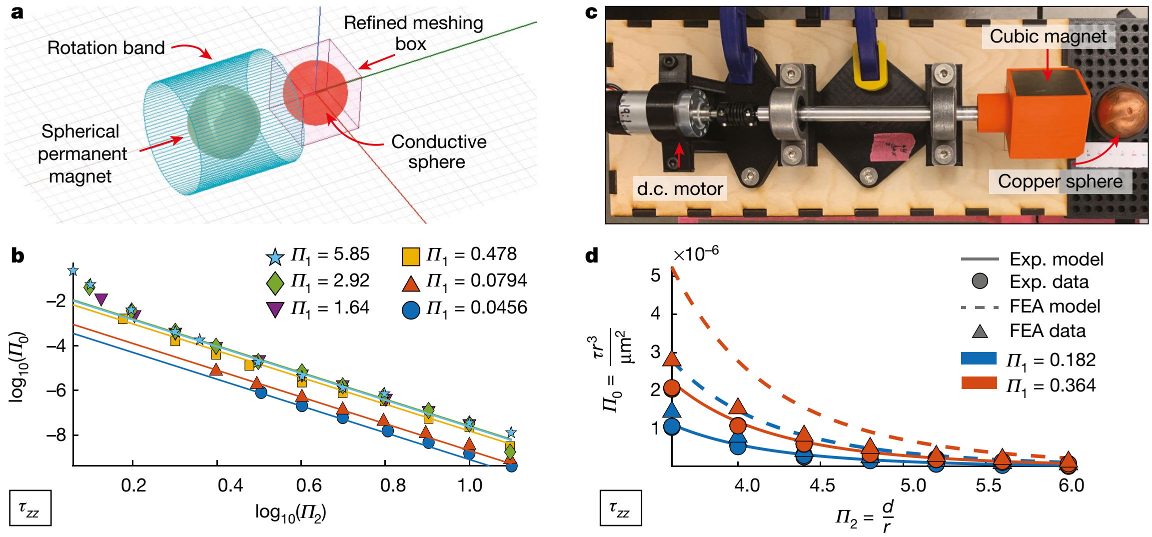

Fig. 2 | Typical numerical and experimental results for force-torque characterization. For clarity, only a subset of the data for a single component τ_{zz} is shown. **a**, Rendering of FEA simulation. **b**, FEA data with unified regression model. **c**, Top view of experimental set-up. **d**, Experimental data with unified regression model. Unified FEA regression model with new FEA data not included in the training set.

ambiguity expressed as a rotation about the z-axis by some γ using a rotation matrix $\mathrm{Rot}_z(\gamma)$. Each source then has three discrete actions ($a \in \{1, 2, 3\}$, respectively) that can be performed on the conductive object, where each action is a specific force-torque wrench with a controllable magnitude:

$$\begin{bmatrix} {}^{w}f \\ {}^{w}\tau \end{bmatrix} \in m^2 \begin{bmatrix} {}^{w}R_{mi} & 0 \\ 0 & {}^{w}R_{mi} \end{bmatrix} \left\{ \begin{bmatrix} 0 \\ 0 \\ \tilde{f}_{zzi} \\ 0 \\ 0 \\ \tilde{\tau}_{zzi} \end{bmatrix}, \begin{bmatrix} 0 \\ 0 \\ \tilde{f}_{zzi} \\ 0 \\ 0 \\ -\tilde{\tau}_{zzi} \end{bmatrix}, \begin{bmatrix} \mathrm{Rot}_z(\gamma) & 0 \\ 0 & \mathrm{Rot}_z(\gamma) \end{bmatrix} \begin{bmatrix} 0 \\ -\tilde{f}_{\rho\phi i} \\ \tilde{f}_{\rho\rho i} \\ -\tilde{\tau}_{\rho z i} \\ 0 \\ 0 \end{bmatrix} \right\} \quad (3)$$

where ${}^{w}R_{mi} = {}^{w}R_{ei}\,{}^{ei}R_{mi}$ and the tilde operator (~) indicates the respective force-torque value when $m = 1$.

With n sources, there are $3n$ possible actions, with m and γ as the control variables in general. Analogous to magnetic manipulation of soft-magnetic objects, superposition does not apply here, so we implement these actions one at a time, for a brief duration of time. To get as close as possible to the desired wrench, we solve the following constrained optimization problem:

$$\begin{aligned} &\underset{i,a,m,\gamma}{\arg\min} \left\| \begin{bmatrix} {}^{w}f_{\mathrm{des}} \\ {}^{w}\tau_{\mathrm{des}} \end{bmatrix} - \begin{bmatrix} {}^{w}f \\ {}^{w}\tau \end{bmatrix} \right\|_Q^2 \\ &\text{subject to} \\ &i \in \{1, \cdots, n\}, \quad a \in \{1, 2, 3\}, \quad m \in [0, m_{\max}], \\ &\quad \gamma \in [-\pi, \pi] \end{aligned} \quad (4)$$

where the Q-norm enables relative weighting between force and torque (that is, relative penalties on position error versus orientation error). We efficiently find the optimal inputs using a parallelized, gradient-based solver.

We first validated our manipulation framework in a numerical simulation of microgravity in which six dipole-field sources surround and dexterously manipulate a copper sphere (see Supplementary Information 6). We performed 3-DOF position control, with and without 3-DOF orientation control (see Fig. 3a–d). Experimental validation was then performed using Omnimagnets[19], which are designed to serve as approximate dipole-field sources, each comprising three co-located and mutually orthogonal electromagnets. A copper sphere floated in a raft in a container of water above four Omnimagnets (see Fig. 3e and Supplementary Information 7), serving as an Earth-based microgravity simulator with 3-DOF mobility in a horizontal plane. We performed 2-DOF position control, with and without 1-DOF orientation control (see Fig. 3f, g).

With our proposed method, 6-DOF manipulation of conductive non-magnetic spheres is achievable. In contrast, 6-DOF manipulation of ferromagnetic objects is only possible for complex geometries[23], with 5-DOF typical of most simple geometries and only 3-DOF achievable for soft-magnetic spheres[1]. The forces and torques generated using the proposed method are likely to be orders of magnitude smaller than those generated using ferromagnetism with comparable parameters, as indicated by the relatively slow manipulation demonstrations of Fig. 3, but they enable manipulation of objects that ferromagnetic methods do not (further discussion in Supplementary Information 8).

Manipulation with six DOF of ferromagnetic objects can be accomplished using eight static electromagnets[24,25], or eight permanent magnets at fixed positions with each having the ability to rotate about an axis orthogonal to its dipole axis[26]. Our numerical simulations showed that six rotating-dipole sources is sufficient for 6-DOF manipulation of conductive spheres; however, this number should not be assumed to be necessary. Since all wrenches have a repulsive force component, when manipulating an unconstrained object, the sources must surround the object to some degree. Analysing the manipulability of different numbers and arrangements of sources is left as an open problem.

In terms of modelling, thus far we have only considered solid spheres. A natural next step would be to consider hollow spheres and other simple geometric objects (such as cuboids or cylinders), which is likely to require more complicated models. It is unclear whether the best approach will be to explicitly model these objects or whether the sphere model can be used in conjunction with learning-based approaches for control. Although we have shown that a simplified approach using canonical positions and actuating one dipole-field source at a time is sufficient to perform dexterous manipulation,

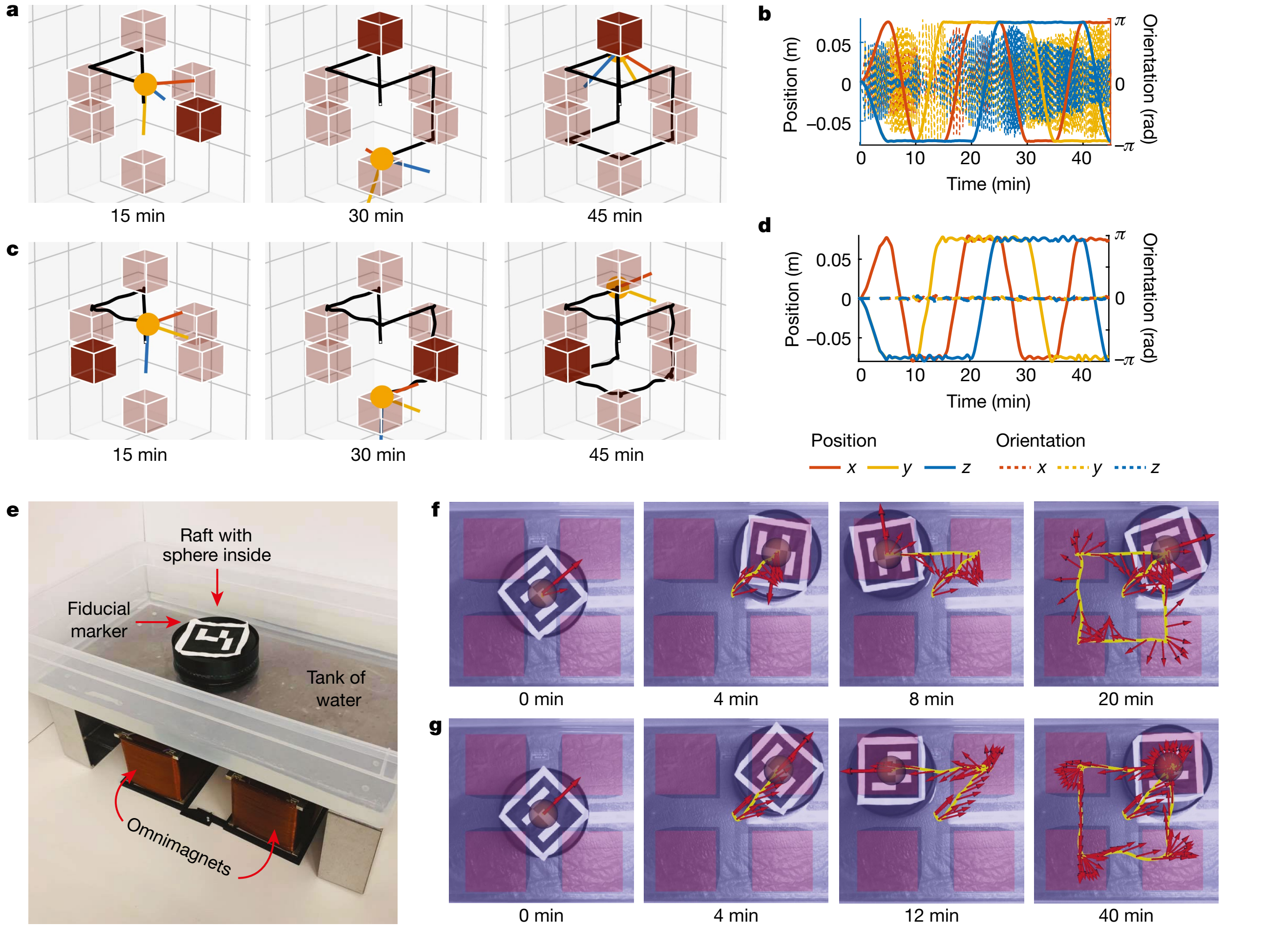

Fig. 3 | Dexterous manipulation of a copper sphere in simulated microgravity. See Supplementary Videos 1–4. **a**, **b**, Numerical simulation with 3-DOF position control along the edges of a cube (the black line is the path taken) and uncontrolled orientation using six dipole field sources (brown cubes, with the highlighted cube indicating the active source at the given instant; **a**), with the resulting 6-DOF pose (**b**). **c**, **d**, Numerical simulation with 6-DOF position and constant-orientation control (**c**), with the resulting 6-DOF pose (**d**). **e**, Experimental set-up with a copper sphere in a raft on water over four Omnimagnets. **f**, Experiments with 2-DOF position control along the edges of a square and uncontrolled orientation (the yellow line is the path taken, and red arrows depict the orientation). **g**, Experiments with 2-DOF position control and 1-DOF orientation control, with sharp turns at the corners.

it is probably suboptimal. A general wrench model for arbitrary sphere positions relative to the rotating dipole, and understanding the nonlinear nature of superposition, are both left as open problems.

Online content

Any methods, additional references, Nature Research reporting summaries, source data, extended data, supplementary information, acknowledgements, peer review information; details of author contributions and competing interests; and statements of data and code availability are available at https://doi.org/10.1038/s41586-021-03966-6.

1. Abbott, J. J., Diller, E. & Petruska, A. J. Magnetic methods in robotics. *Annu. Rev. Control Robot. Auton. Syst.* **3**, 57–90 (2020).
2. Hertz, H. *Miscellaneous Papers* Chapter 2 [transl. Jones, D. E. & Schott, G. A.] (Macmillan, 1896).
3. Griffiths, D. J. *Introduction to Electrodynamics* 4th edition (Cambridge Univ. Press, 2017).
4. Nagel, J. R. Induced eddy currents in simple conductive geometries: mathematical formalism describes the excitation of electrical eddy currents in a time-varying magnetic field. *IEEE Antennas Propag. Mag.* **3**, 81–88 (2018).
5. Youngquist, R. C., Nurge, M. A., Starr, S. O., Leve, F. A. & Peck, M. A. A slowly rotating hollow sphere in a magnetic field: first steps to de-spin a space object. *Am. J. Phys.* **84**, 181–191 (2016).
6. Nurge, M. A., Youngquist, R. C. & Starr, S. O. A thick-walled sphere rotating in a uniform magnetic field: the next step to de-spin a space object. *Am. J. Phys.* **85**, 596–610 (2017).
7. Nurge, M. A., Youngquist, R. C. & Starr, S. O. Drag and lift forces between a rotating conductive sphere and a cylindrical magnet. *Am. J. Phys.* **86**, 443–452 (2018).
8. Sharma, K. K. et al. Space debris reduction using eddy currents. In *2018 Atmospheric Flight Mechanics Conf.*, 3161 (American Institute of Aeronautics and Astronautics, 2018).
9. Reinhardt, B. Z. & Peck, M. A. New electromagnetic actuator for on-orbit inspection. *J. Spacecraft Rockets* **53**, 241–248 (2016).
10. Liu, X., Lu, Y., Zhou, Y. & Yin, Y. Prospects of using a permanent mangetic end effector to despin and detumble an uncooperative target. *Adv. Space Res.* **61**, 2147–2158 (2018).
11. Smith, Y. R., Nagel, J. R. & Rajamani, R. K. Eddy current seperation for recovery of non-ferrous metallic particles: a comprehensive review. *Miner. Eng.* **133**, 149–159 (2019).
12. Buckingham, E. On physically similar systems; illustrations of the use of dimensional equations. *Phys. Rev.* **4**, 345 (1914).
13. Shan, M., Guo, J. & Gill, E. Review and comparison of active space debris capturing and removal methods. *Prog. Aerosp. Sci.* **80**, 18–32 (2016).
14. Mark, C. P. & Kamath, S. Review of active space debris removal methods. *Space Policy* **47**, 194–206 (2019).
15. Kessler, D. J., Johnson, N. L., Liou J. C. & Matney, M. The Kessler syndrome: implications to future space operations. *Adv. Astronaut. Sci.* **137**, AAS 10-016 (2010).
16. Opiela, J. N. A study of the material density distribution of space debris. *Adv. Space Res.* **43**, 1058–1064 (2009).
17. Pelrine, R. et al. Diamagnetically levitated robots: an approach to massively parallel robotic systems with unusual motion properties. *IEEE Int. Conf. Robotics and Automation*, 739–744 (2012).
18. Mirica, K. A., Ilievski, F., Ellerbee, A. K., Shevkoplyas, S. S. & Whitesides, G. M. Using magnetic levitation for three dimensional self-assembly. *Adv. Mater.* **23**, 4134–4140 (2011).

19. Petruska, A. J. & Abbott, J. J. Omnimagnet: an omnidirectional electromagnet for controlled dipole-field generation. *IEEE Trans. Magn.* **50**, 8400410 (2014).
20. Wright, S. E., Mahoney, A. W., Popek, K. M. & Abbott, J. J. The spherical-actuator-magnet manipulator: a permanent-magnet robotic end-effector. *IEEE Trans. Robot.* **33**, 1013–2924 (2017).
21. Petruska, A. J. & Abbott, J. J. Optimal permanent-magnet geometries for dipole field approximation. *IEEE Trans. Magn.* **49**, 811–819 (2013).
22. Lynch, K. M. & Park, F. C. *Modern Robotics: Mechanics, Planning, and Control* (Cambridge Univ. Press, 2017).
23. Diller, E., Giltinan, J., Lum, G. Z., Ye, Z. & Sitti, M. Six-degree-of-freedom magnetic actuation for wireless microrobotics. *Int. J. Robot. Res.* **35**, 114–128 (2016).
24. Kummer, M. P. et al. OctoMag: an electromagnetic system for 5-DOF wireless micromanipulation. *IEEE Trans. Robot.* **26**, 1006–1017 (2010).
25. Petruska, A. J. & Nelson, B. J. Minimum bounds on the number of electromagnets required for remote magnetic manipulation. *IEEE Trans. Robot.* **31**, 714–722 (2015).
26. Ryan, P. & Diller, E. Magnetic actuation for full dexterity microrobotic control using rotating permanent magnets. *IEEE Trans. Robot.* **33**, 1398–1409 (2017).

Data availability

All data generated and scripts for analyses during this study are included in the published article and can be found using the following link: https://osf.io/uk3rx/.

Acknowledgements This work was supported by the National Science Foundation under grants 1841845 and 1846341.

Author contributions J.J.A. and T.H. proposed the research. All authors participated in the planning of the article. L.N.P. and J.J.A. performed the dimensional analysis and designed the experiments to characterize force-torque. L.N.P. and J.L.B.A. performed the numerical simulations to characterize force-torque. G.F.T. and T.H. designed the numerical microgravity manipulation simulator and control scheme, and integrated the controller into the experimental manipulation system. L.N.P., G.F.T. and A.P. designed and performed the manipulation experiments. L.N.P., G.F.T. and J.J.A drafted the manuscript. All other authors performed a critical revision.

Competing interests J.J.A. has patents and patents pending on electromagnet and permanent-magnet devices designed to generate rotating magnetic dipole fields. The other authors declare no competing interests.

Additional information

Supplementary information The online version contains supplementary material available at https://doi.org/10.1038/s41586-021-03966-6.

Correspondence and requests for materials should be addressed to Jake J. Abbott.

Peer review information *Nature* thanks Eric Diller and the other, anonymous, reviewer(s) for their contribution to the peer review of this work.

Dexterous Magnetic Manipulation of Conductive Non-magnetic Objects: Supplementary Information

Lan N. Pham[*], Griffin F. Tabor[†], Ashkan Pourkand[†], Jacob L. B. Aman[‡], Tucker Hermans[†], and Jake J. Abbott[*]

Contents

[*]Department of Mechanical Engineering, University of Utah, Salt Lake City, UT 84112, USA
[†]School of Computing, University of Utah, Salt Lake City, UT 84112, USA
[‡]Lawrence Livermore National Laboratory, Livermore, CA 94550, USA

1 Dimensional Analysis

When using the Buckingham Π theorem to characterize induced force f (units N) in a given canonical position, we first enumerate the independent variables that may affect force: the radius of the conductive sphere r (units m); the magnitude of the dipole $m = \|\boldsymbol{m}\|$ (units A·m^2); the magnitude of the angular velocity of the dipole $\omega = \|\boldsymbol{\omega}\|/(2\pi)$ (which we chose to represent in units Hz rather than units rad/s typical of $\boldsymbol{\omega}$); the permeability of the environment μ (units N·A^{-2}); the distance from the dipole to the center of the conductive sphere $d = \|\boldsymbol{d}\|$ (units m), and the conductivity of the sphere σ (units S·m^{-1} = N^{-1}· m^{-2}·s·A^2). Thus, there are seven parameters describing the problem (one dependent and six independent). These quantities collectively comprise four dimensions (m, N, s, A), as described in Table 1. The Buckingham Π theorem tells us that the number of parameters, 7, minus the number of dimensions, 4, equals the number of dimensionless Π groups, 3, that can be used to characterize the underlying physics of the system. Our choice of Π groups is provided in Table 1. These Π groups are not unique, but we can check that our proposed Π groups are valid by constructing two matrices. The first is a matrix A where each row corresponds to a dimension, each column corresponds to a parameter, and each element contains the power of the dimensions in the respective parameters. The second is a matrix B where the rows correspond to the parameters (ordered as in A), each column corresponds to a Π group, and each element contains the power of the parameters in the respective Π groups. A valid set of Π groups is one in which B has full column rank and AB is a zero matrix:

$$A = \begin{array}{c} \\ \mathrm{m} \\ \mathrm{N} \\ \mathrm{s} \\ \mathrm{A} \end{array} \begin{array}{c} \begin{array}{ccccccc} f & r & m & \omega & \mu & d & \sigma \end{array} \\ \begin{bmatrix} 0 & 1 & 2 & 0 & 0 & 1 & -2 \\ 1 & 0 & 0 & 0 & 1 & 0 & -1 \\ 0 & 0 & 0 & -1 & 0 & 0 & 1 \\ 0 & 0 & 1 & 0 & -2 & 0 & 2 \end{bmatrix} \end{array}, \quad B = \begin{array}{c} \\ f \\ r \\ m \\ \omega \\ \mu \\ d \\ \sigma \end{array} \begin{array}{c} \begin{array}{ccc} \Pi_0 & \Pi_1 & \Pi_2 \end{array} \\ \begin{bmatrix} 1 & 0 & 0 \\ 4 & 2 & -1 \\ -2 & 0 & 0 \\ 0 & 1 & 0 \\ -1 & 1 & 0 \\ 0 & 0 & 1 \\ 0 & 1 & 0 \end{bmatrix} \end{array} \tag{S1}$$

The process used for induced force is repeated for induced torque τ (units N·m), with changes only to column 1 of A and column 1 of B:

$$A = \begin{array}{c} \\ \mathrm{m} \\ \mathrm{N} \\ \mathrm{s} \\ \mathrm{A} \end{array} \begin{array}{c} \begin{array}{ccccccc} \tau & r & m & \omega & \mu & d & \sigma \end{array} \\ \begin{bmatrix} 1 & 1 & 2 & 0 & 0 & 1 & -2 \\ 1 & 0 & 0 & 0 & 1 & 0 & -1 \\ 0 & 0 & 0 & -1 & 0 & 0 & 1 \\ 0 & 0 & 1 & 0 & -2 & 0 & 2 \end{bmatrix} \end{array}, \quad B = \begin{array}{c} \\ \tau \\ r \\ m \\ \omega \\ \mu \\ d \\ \sigma \end{array} \begin{array}{c} \begin{array}{ccc} \Pi_0 & \Pi_1 & \Pi_2 \end{array} \\ \begin{bmatrix} 1 & 0 & 0 \\ 3 & 2 & -1 \\ -2 & 0 & 0 \\ 0 & 1 & 0 \\ -1 & 1 & 0 \\ 0 & 0 & 1 \\ 0 & 1 & 0 \end{bmatrix} \end{array} \tag{S2}$$

In the case of a permanent magnet, the dipole strength will be a product of the volume of the magnet and the average magnetization of the material. In the case of an electromagnet, the dipole strength will be a function of applied electrical current, and can often be modeled as linear with respect to current [1]. In both cases, the distance d is measured from the center of the magnet to the center of the conductive sphere.

Although the magnetic permeability of the environment, μ, is an independent variable in general, in practice it will always be the permeability of free space, $\mu = \mu_0$. If we were to consider special cases in which the interstitial space is filled with a magnetic material such as a ferrofluid [2], forces imparted by the environment would likely dominate the eddy-current-induced forces of interest here.

The Buckingham Π theorem tells us that the maximum number of dimensionless terms that will be required to characterize the physics of our problem, but it does not necessarily tell us the minimum number. In some cases, dimensionless Π groups can be further combined to form new dimensionless groups. We hypothesized that it may be possible to express the dimensionless quantity Π_0/Π_1 as a function of a single dimensionless independent variable Π_2.

This hypothesis was derived from the hypothesis that both f and τ would be linear with respect to ω. However, during the numerical studies described in Supplementary Information 2, we determined that this hypothesis was not correct.

2 Numerical Characterization of Force and Torque

In this section we describe how to setup the finite-element-analysis (FEA) program Ansys Electronics Desktop 2019 R2 Maxwell, in order to simulate the eddy-current-induced forces and torques on conductive copper and aluminum spheres due to a rotating magnetic dipole. The order described below is in the same order as they would appear in the "Project Manager". Once the setup is performed for each configuration, force-torque data can be obtained by performing "Analysis All". A total of 642 FEA simulations were performed for all parameters outlined in Table S1. Using these FEA simulations we determined the non-negligible force and torque components shown in Fig. 1.

Solution Type: In order to perform transient analysis with a rotating dipole source, one has to go to "Maxwell 3D", select "Solution Type" and choose "Transient".

3D Components: Using Coordinate System = Global, we modeled the magnetic dipole source as a spherical NdFeB grade-N48 rare-earth magnet. When building the spherical magnet, it has the following model properties: Command = Create Sphere, Coordinate System = Global, Center Position = [0, 0, 0] (all model coordinates are provided in units of millimeters). The center of the sphere should be located at the center of the Global coordinate system. The material property for the spherical magnetic dipole has the following material properties: Relative Permeability $\mu_m/\mu_0 = 1.04$, Bulk Conductivity $\sigma = 714286$ S/m, Magnetic Coercivity $H_{cm} = 1055931$ A/m (in Ansys this is entered as a negative value), Core Loss = None, Composition = Solid, Mass Density = 7550 kg/m^3, Young's Modulus = Undefined, Poisson's ratio = Undefined, and Thermal Modifier = None. The radius of the magnet was determined to achieve the desired dipole strength m, which is equal to the product of the remanent magnetization M_r and the volume of the sphere. The magnetization model used is depicted in Fig. S1. From this model, we see that we can compute $M_r = H_{cm}\mu_m/\mu_0$. Also note that the default magnetization in Ansys is in the x direction.

To enable the dipole-source rotation, a regular polyhedron was created surrounding the magnet with the following model properties: Coordinate = Global, Center Position = [0, -45, 0], Start Position [0, 0, 0], Axis = Y, Height = 90, and Number of Segments = 100.

To model the conductive sphere, a new coordinate system was created, which enables all relative sphere components to move together and enables output force-torque values to be referenced relative to the conductive-sphere frame. The model for the conductive sphere has the following properties: Command

Copper: $\sigma = 5.8 \times 10^7$ S/m						Aluminum: $\sigma = 3.8 \times 10^7$ S/m					
m (A·m^2)	r (mm)	ω (Hz)	d (mm)	Π_1 —	Π_2 —	m (A·m^2)	r (mm)	ω (Hz)	d (mm)	Π_1 —	Π_2 —
104	25	1	80	0.0456	3.20	208	40	1	100	0.0794	2.50
		2.5	100	0.114	4.00			2	125	0.153	3.12
		5	125	0.228	5.00			4	160	0.306	4.00
		10	160	0.456	6.40			6	200	0.458	5.00
		20	200	0.911	8.00			8	250	0.611	6.25
		30	250	1.37	10.0			10	315	0.764	7.88
		40	315	1.82	12.6			12	400	0.917	10.0
		50		2.28				14	500	1.07	12.5
		60		2.73				16		1.23	
		70		3.19				18		1.38	
		80		3.64				20		1.52	
		90		4.10							
		100		4.56							
312	150	1	200	1.64	1.33	208	100	1	150	0.478	1.50
		2	230	3.28	1.53			2	200	0.955	2.00
		3	300	4.92	2.00			4	250	1.91	2.50
		4	375	6.56	2.50			6	300	2.87	3.00
		5	475	8.20	3.17			8	400	3.82	4.00
		6	600	9.94	4.00			10	500	4.77	5.00
		7	750	11.5	5.00			12	630	5.73	6.30
		8	950	13.1	6.33			14	800	6.69	8.00
		9	1200	14.8	8.00			16	1000	7.64	10.0
		10	1500	16.4				18	1250	8.60	12.5
								20		9.55	
104	200	1	250	2.92	1.25	312	350	1	400	5.85	1.14
		1.5	315	4.37	1.57			1.25	440	7.31	1.25
		2	400	5.83	2.00			1.5	550	8.77	1.57
		2.5	500	7.29	2.50			1.75	700	10.2	2.00
		3	630	8.75	3.15			2	880	11.7	2.51
		3.5	800	10.2	4.00			2.25	1100	13.2	3.14
		4	1000	11.7	5.00			2.5	1400	14.6	4.00
		4.5	1250	13.1	6.25			2.75	1750	16.1	5.00
		5	1600	14.6	8.00			3	2200	17.5	6.29
		5.5	2000	16.0	10.0			3.25	2780	19.0	7.94
		6	2500	17.5	12.50			3.5	3500	20.5	10.00
									4400		12.6

Table S1: **Summary of FEA parameters for force and torque characterization.** For each combination of σ, m, and r, a set of ω were tested, and at each ω a set of d were tested. This resulted in a variety of Π_1 values, and at each Π_1 value a variety of Π_2 values. These same values were used for both the z and ρ configurations.

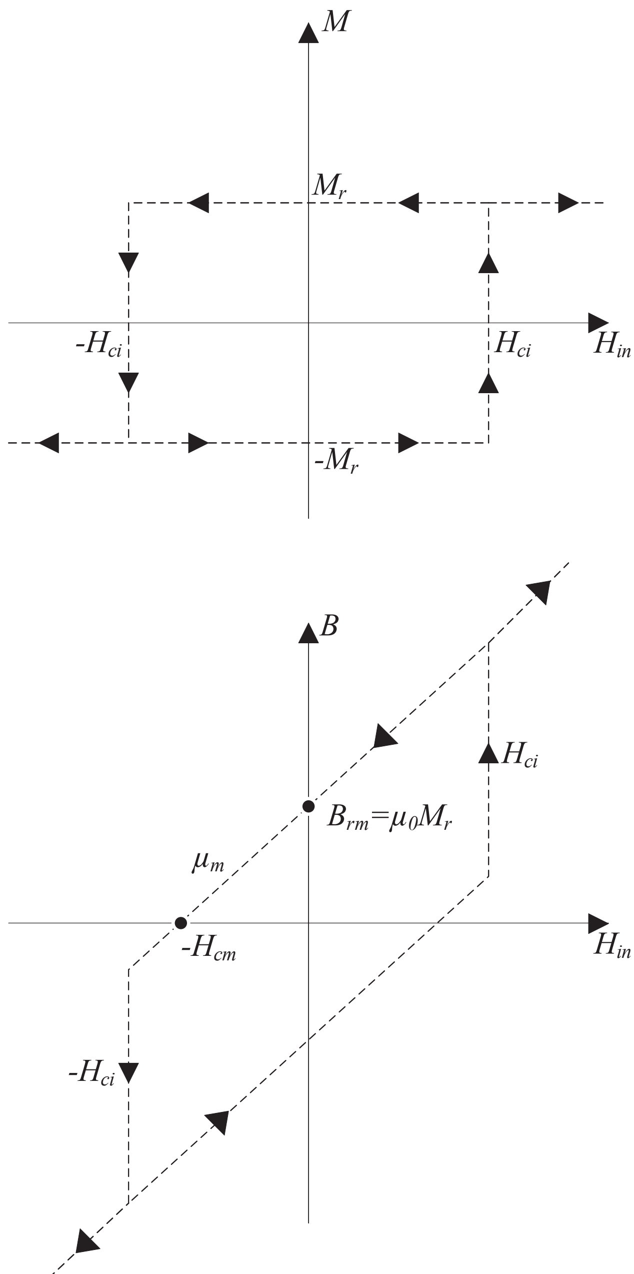

Figure S1: **Magnetization model for permanent magnets used in Ansys Maxwell.** H_{in} is the internal field in the material (units A·m^{-1}), H_{ci} is the coersive internal field in the material (units A·m^{-1}), H_{cm} is the magnetic coersivity (units A·m^{-1}), M is the magnetization (units A·m^{-1}), M_r is the remanent magnetization (units A·m^{-1}), B is the flux density (units T), B_r is the remanent flux density (units T), and μ_0 is the permeability of free space (units N·A^{-2} = T·m·A^{-1}).

= Create Sphere, Coordinate System = Sphere, Center Position = [0, 0, 0], and the desired radius. A conductive aluminum sphere has the following material properties: Relative Permeability = 1.000021, Bulk Conductivity = 38000000 S/m, Magnetic Coercivity = 0, Core Loss = None, Composition = Solid, Mass Density = 2689 kg/m^3, Young Modulus = 69000000000, Poisson's Ratio = 0.31, and Thermal Modifier = None. A conductive copper sphere has the following material properties: Relative Permeability = 1, Bulk Conductivity = 58000000 S/m, Magnetic Coercivity = 0, Core Loss = 0, Composition = Solid, Mass Density = 8933 kg/m^3, Young's Modulus = 120000000000, Poisson's Ratio = 0.38, Thermal Modifier = None.

A cubic box was created to surround the conductive sphere for refined meshing. The model has the following model properties: Command = Create Box, Coordinate System = Sphere, with position and dimension of the box set such that the box was centered on the conductive sphere and had a side length that is 1% larger than the diameter of the sphere. It has material property = air.

Model: Dipole rotation is implemented by right selecting the polyhedron model and assigning a Band. This generates a "MotionSetup" option under Model, which one can use to configure the following motion parameters: Motion Type = Rotation, Coordinate System = Global, Axis = Y, Direction = Positive, Inital Position = 0 deg, Has Rotation Limit = unchecked, and Non Cylindrical = unchecked. Under the "Mechanical" tab one can update the angular velocity to the desired frequency of rotation. This automatically generates a CylindericalGap mesh and the axis of the rotation vector must be along the same axis as the length of the polyhedron.

Parameters: Output parameters are produced by right selecting the conductive sphere and creating parameters for force, torque in x, torque in y, and torque in z, with respect to the conductive sphere coordinate system. A single force parameter will automatically produce outputs for all x, y, z directions. Depending on the relative placement of the conductive sphere to the dipole rotation axis, one can transform the Cartesian coordinates to our proposed cylindrical coordinate system.

Mesh operations: When assigning Mesh parameters, one must first right select the object and then select "Assign Mesh Operation". All mesh configurations have the following mesh properties: Type = Length Based, Region = Inside Selection, Enable = checked, Restrict Length = checked, and Restricted Max Elems = checked. Max Length and Max Elems are different for each object.

The mesh for the spherical permanent magnet is the mesh for the polyhedron. The polyhedron has Max Length = 5 mm and Max Elements = 5000.

For the conductive sphere and its cubic box, the Max Length and Max Elems are scaled proportionally to the smallest sphere radius of 25 mm for consistent mesh properties across all conductive spheres. For the conductive sphere the Max Length = r/5 mm (where r is in units mm) and Max Elems = $4000r$. The mesh for the cubic box of air is an additional mesh operation for the conductive sphere and has Max length = r/5 mm and Max Elems = $50000r$.

Analysis setup: The Analysis setup consists of Stop Time and Time Step for each FEA and are listed here with respect to $\omega = 1$ Hz and Time Step = 1 ms. For conductive spheres with radii 25 mm and 40 mm the Stop Time = 2.5 s, for radii 100 mm and 150 mm the Stop Time = 4 s, and for radii 200 mm and 350 mm the Stop Time = 5 s. Larger spheres had longer Stop Time in order to allow the FEA to reach steady state. For all other values of ω, the Analysis Setup parameters were scaled proportional to each frequency in order to maintain the same number of data points and number of dipole rotations. For examples, for a conductive sphere with 25 mm radius, at $\omega = 2$ Hz, values would be updated to Stop Time = 1.5 s and Time Step = 0.5 ms.

Results: Under "Results", create two transients reports of rectangular plots for force and torque output on the conductive sphere. Data is saved for each time step of the FEA.

Eddy-current configuration: To include the effects of eddy current on the conductive sphere, go to Maxwell 3D, select Excitations, select Set Eddy Effects, and check the box for the conductive sphere.

Model Parameters for Analysis: Once the setup is complete, one can perform "Analysis All" in order to start the FEA. While iterating through all parameters outlined in Table S1, FEAs were automated through the use of a Python script using ANSYS Maxwell "Automation". The steady-state data was obtained by averaging the last dipole rotation.

3 Model Derivation

When visualizing the resulting non-dimensional Π groups for the FEA data (see column 1 of Figs. S2 and S3), we observed that at relatively far distances ($\Pi_2 > 1.5$, approximately), the relationship between $\log_{10}(\Pi_0)$ and $\log_{10}(\Pi_2)$, for a given Π_1, can be accurately described by a linear model of the form

$$\log_{10}(\Pi_0) = \xi \log_{10}(\Pi_2) + \psi \tag{S3}$$

where ξ is a slope and ψ is an intercept term in the log-log scale. We performed least-squares regression, using MATLAB's 2020a Curve Fitting Toolbox, on each of the data sets corresponding to a specific value of Π_1, including all data with $\Pi_2 > 1.5$. We observed that the resulting slopes were very close to $\xi = -6$ for both torques, and $\xi = -7$ for all three forces. Since these values are analogous to what is expected from magnetic torque and force imparted by a magnetic dipole on a soft-magnetic object—due to field strength and thus magnetization decaying as $\propto d^{-3}$, torque being the product of magnetization and field strength (i.e., $\propto d^{-3}d^{-3} = d^{-6}$), and force being the product of magnetization and the spatial derivative of the field (i.e., $\propto d^{-3}d^{-4} = d^{-7}$) [1]—we fixed those values and then redid the least-squares regression, using the following settings: "StartPoint" set to $[-1]$ and "Upper" bound set to $[0]$.

We then determined that the intercept term could be described as a function of Π_1 with four free parameters, c_0–c_3 (see column 2 of Figs. S2 and S3):

$$\psi = \log_{10}(c_0\Pi_1)c_1{\Pi_1}^{c_2} + c_3 \tag{S4}$$

This regression used "StartPoint" set to $[0.5,\ 1,\ -1,\ -1]$ and "Lower" bound set to $[0,\ 0,\ -\inf,\ -\inf]$. We let $\xi = c_4$ to create a consistent naming convention. Finally, after substituting Eq. S4 into Eq. S3 and taking the inverse logarithm of both sides of Eq. S3 we obtained the unified model given as Eq. 2. From this modeling, the coefficients for the FEA-based unified model derived from each of the non-zero forces and torques are provided under "Finite-element-analysis (FEA)" in Table S2. When calculating the error between the FEA-based model and the FEA data points, across all configurations and force-torque components, the median error is $+0.04\%$ and the interquartile range is $[-3\%,\ +2\%]$.

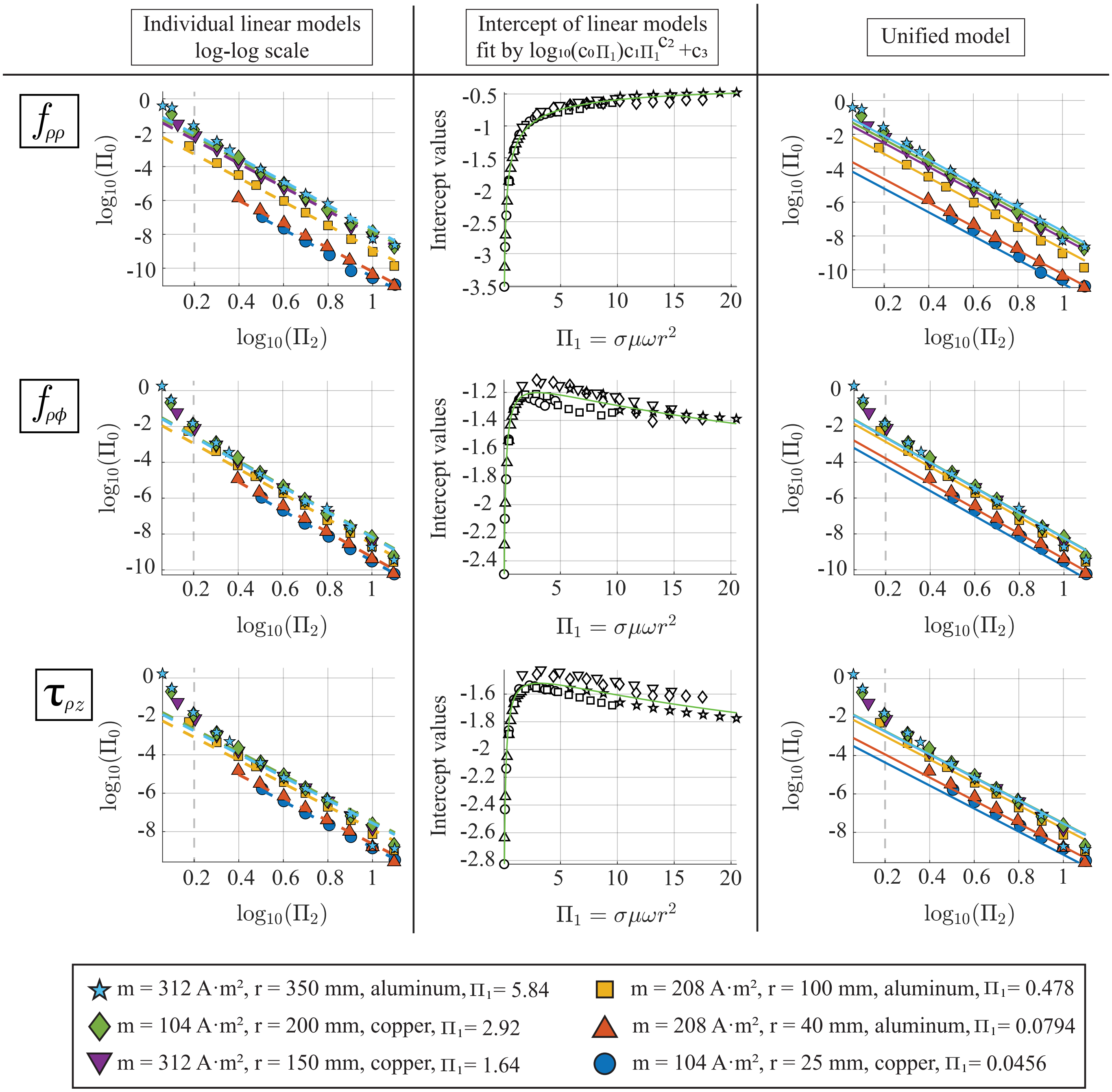

Figure S2: **Far-field model fitting for FEA results in the ρ configuration.** (Left) Linear models are fit to $\log_{10}(\Pi_0)$ vs. $\log_{10}(\Pi_2)$ for individual Π_1 values, with a slope of -7 for forces and -6 for torques, using only results $\log_{10}(\Pi_2) > 0.2$. For clarity, only the lowest ω value from each set of m, r, and σ are shown. (Center) The resulting intercept values are fit with the model $\log_{10}(c_0\Pi_1)c_1{\Pi_1}^{c_2} + c_3$, using the complete set of Π_1 values. (Right) The final unified far-field model projected on the original data.

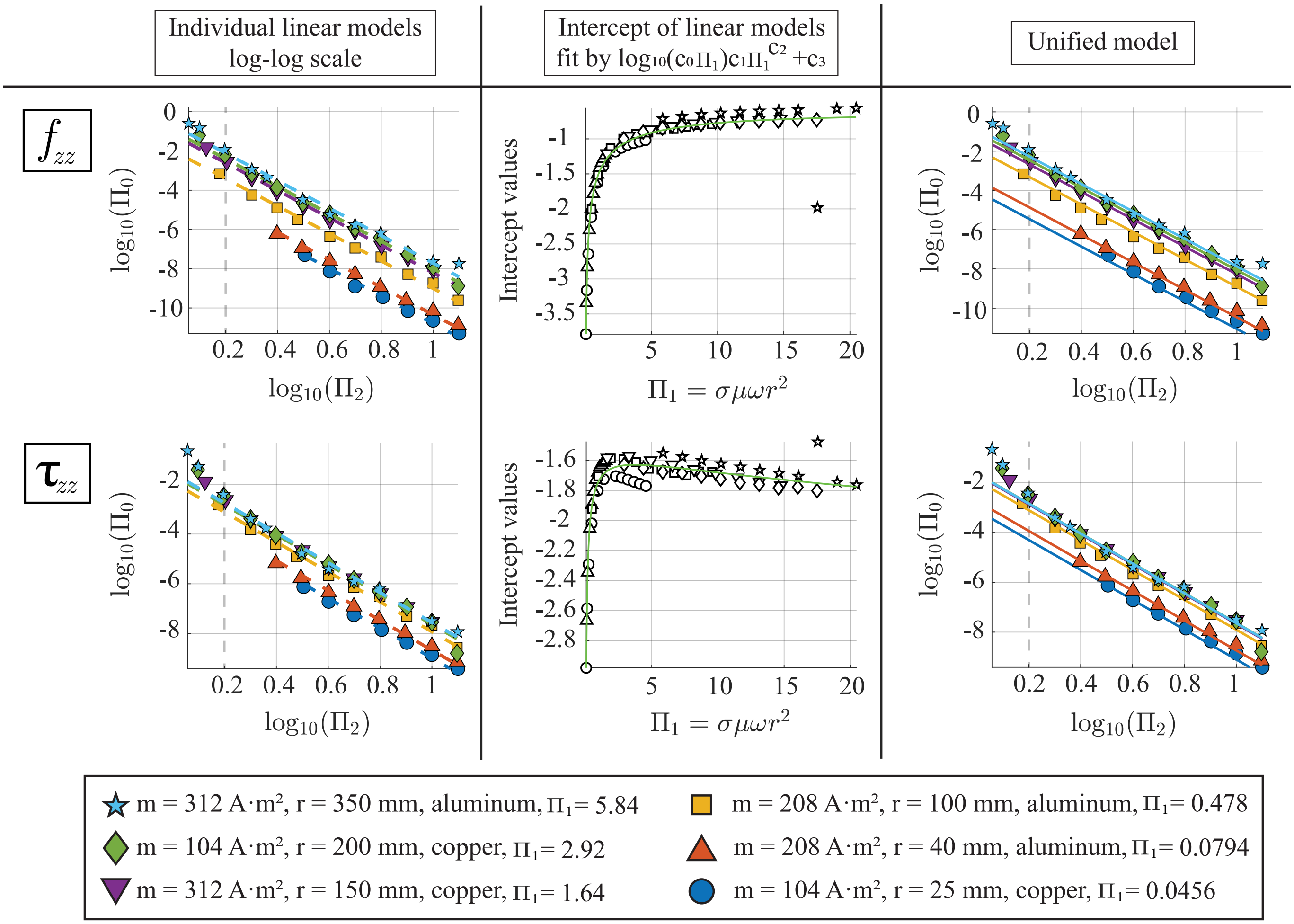

Figure S3: **Far-field model fitting for FEA results in the z configuration.** (Left) Linear models are fit to $\log_{10}(\Pi_0)$ vs. $\log_{10}(\Pi_2)$ for individual Π_1 values, with a slope of -7 for forces and -6 for torques, using only results $\log_{10}(\Pi_2) > 0.2$. For clarity, only the lowest ω value from each set of m, r, and σ are shown. (Center) The resulting intercept values are fit with the model $\log_{10}(c_0\Pi_1)c_1{\Pi_1}^{c_2} + c_3$, using the complete set of Π_1 values. (Right) The final unified far-field model projected on the original data.

f, τ	Coefficients					Adj. R^2
Finite-element-analysis (FEA)						
	c_0	c_1	c_2	c_3	c_4	
f_{zz}	430	2.95	-0.101	-9.26	7	0.969
τ_{zz}	6840	3.00	-0.0986	-13.2	6	0.974
$f_{\rho\rho}$	266	2.60	-0.101	-7.65	7	0.981
$f_{\rho\phi}$	6040	3.45	-0.102	-14.3	7	0.963
$\tau_{\rho z}$	8100	3.60	-0.0985	-15.7	6	0.928
Experimental						
f, τ	Coefficients					Adj. R^2
	c_0	c_1	c_2	c_3	c_4	
f_{zz}	467	2.81	-0.0969	-9.75	7	0.996
τ_{zz}	6900	3.35	-0.0990	-14.9	6	0.999
$f_{\rho\rho}$	282	3.20	-0.0980	-9.41	7	0.919
$f_{\rho\phi}$	5870	3.49	-0.0973	-14.6	7	0.997
$\tau_{\rho z}$	8000	3.40	-0.0928	-15.0	6	0.999

Table S2: **Model coefficients derived from FEA and experiments.** Note, c_4 was fixed based on pilot studies. Only data with $\Pi_2 > 1.5$ were used to derive the model and to compute the adjusted R^2 values.

For all FEA simulations, the magnetic permeability of the environment, μ, was constant and equal to the permeability of free space, $\mu_0 = 4\pi \times 10^{-7}\,\mathrm{N{\cdot}A^{-2}}$. In theory, if Π_1 and Π_2 were kept constant while μ was varied, then the dimensional analysis would expect the same values for Π_0. The results, however, are more complex because increasing μ effectively turns the environment from free space into a kind of ferrofluid. That ferrofluid environment would experience magnetic forces that would be imparted on the conductive sphere, and the resulting forces of the FEA simulation would be the summation of those forces and the eddy-current-induced forces of interest here. Consequently, we do not recommend attempting to apply our model to environments other than those with $\mu \approx \mu_0$.

4 Experimental Verification of Force and Torque

Experimental verification was performed using the setup shown in Fig. 2c. It comprised a DC motor with a 1200 count incremental optical encoder (#4751, Pololu) and a 19:1 gear reduction rotating a 51 mm cubic NdFeB grade-N42 permanent magnet (BY0Y0Y0, K&J Magnetics) with dipole strength of 138 A·m^2, and a solid 25-mm-radius copper sphere mounted on top of a nonmagnetic 6-DOF force-torque sensor (Nano17 Titanium, ATI Industrial Automation). The copper sphere and force-torque sensor were placed on a non-magnetic and nonconductive 3D-printed peg board with 10 mm spaced holes, which enabled the sphere to be placed along the desired z or ρ axes consistently. The pegboard was placed on a separate table from the motor to mitigate vibrations from the motor being picked up by the force-torque sensor. The center of the sphere and the center of the magnet were in the same horizontal plane.

The force-torque sensor was calibrated for SI-8-0.05, in which Fx and Fy have a ± 8 N range with 1.466 mN resolution, Fz has a ± 14.1 N range with 8.241 mN resolution, and Tx, Ty, and Tz have a ± 50 N·mm range with 6.868 mN·mm resolution. Data was recorded using the sensor's ATIDAQFT.net program with the sampling rate set to 1000 Hz.

In the motor-magnet system, the magnet was fitted inside a 3D-printed housing, which was rigidly connected to a long aluminum shaft (supported by two pillow-block bearings), which was connected to the motor via a flexible shaft coupling. The closest face of the motor was 268 mm away from the center of the magnet, which mitigated interaction between the magnet and the motor and also mitigated influence of the motor's magnetic field on the copper sphere. Both the copper sphere and motor systems were raised 170 mm above the surface of each respective table to mitigate interactions between any ferrous or conductive material within the tables. The motor system was tightly clamped to the table to help minimize shaking due to the magnet rotating at high speeds.

For the ρ configuration, the copper sphere was placed at distances (between the center of the sphere and the center of the magnet) in the range 90–150 mm, whereas the z configuration considered distances in the range 70–150 mm (see Tables S3 and S4).

For each configuration (i.e., position and frequency), force-torque sensor data were collected, each comprising 25 s of data. Approximately the first 8 s of data was with the magnet static; this was used to remove any DC bias from the sensor. Next, the magnet was rotated at the desired frequency for the remaining time period. The force-torque sensor experienced the effect of magnet rotation as an application of force and torque on the mounted copper sphere. In post-processing, a discrete-time implementation of a unit-DC-gain first-order low-pass filter with a time constant of 2 s was applied to the data. After the filter's output had reached steady-state (i.e., after at least 10 s), the average force and torque values across 1 s were used to represent that data run. The methodology described above formed a single block of data. Such a block was repeated four more times, giving a total of five runs at each configuration.

The largest forces and torques were produced when the dipole source was rotating at 8 Hz and when the copper sphere was at the shortest distance. In the $\pm z$ configuration the shortest distance is 70 mm with the largest force equaling 0.0773 N in the z direction and the largest torque equaling 0.0141 N·m in the z direction. In the ρ configuration the shortest distance is at 90 mm with the largest force equaling 0.1419 N in the ϕ direction and the largest torque equaling -0.0063 N·m in the z direction.

All experimental data points are shown in Figs. S4 and S5. Note that at the largest distances (i.e., largest Π_2 values) and smallest rotation frequencies (i.e., smallest Π_1 values) the forces measured are near the sensing resolution of the sensor, leading to a poor signal-to-noise ratio. Using the same procedure outlined in Supplementary Information 3, all experimental data points were used to derive the experimental-based model and corresponding adjusted R^2 values provided under "Experimental" in Table S2. Using MATLAB's Curve Fitting Toolbox, the regression used "StartPoint" set to the FEA-based coefficients, "Lower" bound set to [0, 0, -inf, -inf], and "Upper" bound set to [inf, inf, 0, inf]. When calculating the error between the experimental-based model and the experimental points, across all configurations and force-torque components, the median error is $+0.03\%$ and the interquartile range is $[-1\%, +2\%]$.

σ (S/m)	m (A·m^2)	r (m)	ω (Hz)	d (mm)	Π_1 —	Π_2 —
Copper 5.8×10^7	138	25	4	70	0.182	2.8
			5	80	0.228	3.2
			6	90	0.273	3.6
			7	100	0.319	4.0
			8	110	0.365	4.4
				120		4.8
				130		5.2
				140		5.6
				150		6.0

Table S3: **Summary of experimental parameters for force and torque characterization in the z configuration.** Keeping σ, m, and r fixed, a set of ω were tested, and at each ω a set of d were tested. This resulted in five Π_1 values, and at each Π_1 value nine Π_2 values.

σ (S/m)	m (A·m^2)	r (m)	ω (Hz)	d (mm)	Π_1 —	Π_2 —
Copper 5.8×10^7	138	25	4	90	0.182	3.6
			5	100	0.228	4.0
			6	110	0.273	4.4
			7	120	0.319	4.8
			8	130	0.365	5.2
				140		5.6
				150		6.0

Table S4: **Summary of experimental parameters for force and torque characterization for the ρ configuration.** Keeping σ, m, and r fixed, a set of ω were tested, and at each ω a set of d were tested. This resulted in five Π_1 values, and at each Π_1 value seven Π_2 values.

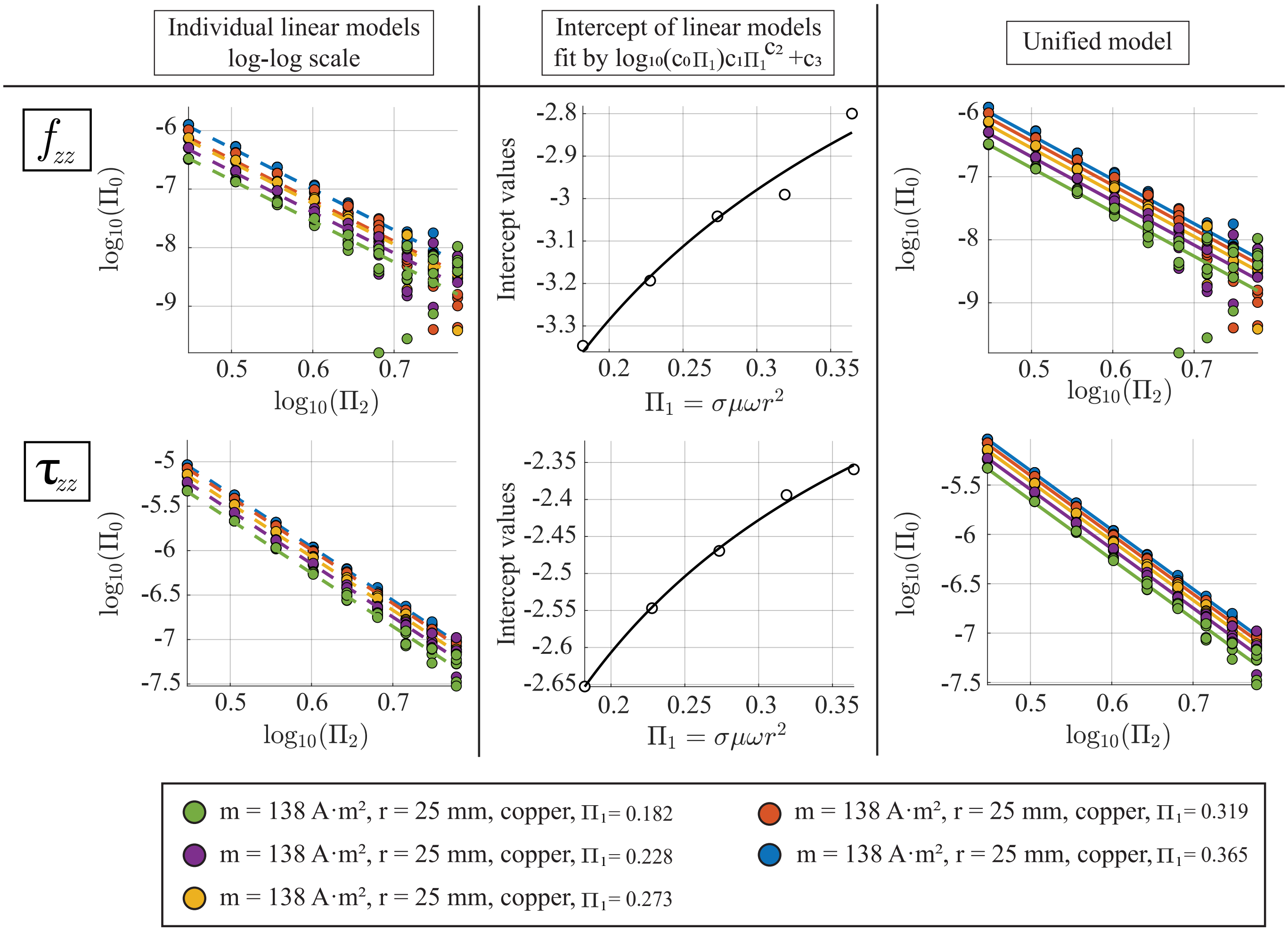

Figure S4: **Far-field model fitting for experimental results in the z configuration.** (Left) Linear models are fit to $\log_{10}(\Pi_0)$ vs. $\log_{10}(\Pi_2)$ for individual Π_1 values, with a slope of -7 for forces and -6 for torques. For clarity, only the lowest ω value from each set of m, r, and σ are shown. (Center) The resulting intercept values are fit with the model $\log_{10}(c_0\Pi_1)c_1{\Pi_1}^{c_2} + c_3$, using the complete set of Π_1 values. (Right) The final unified far-field model projected on the original data.

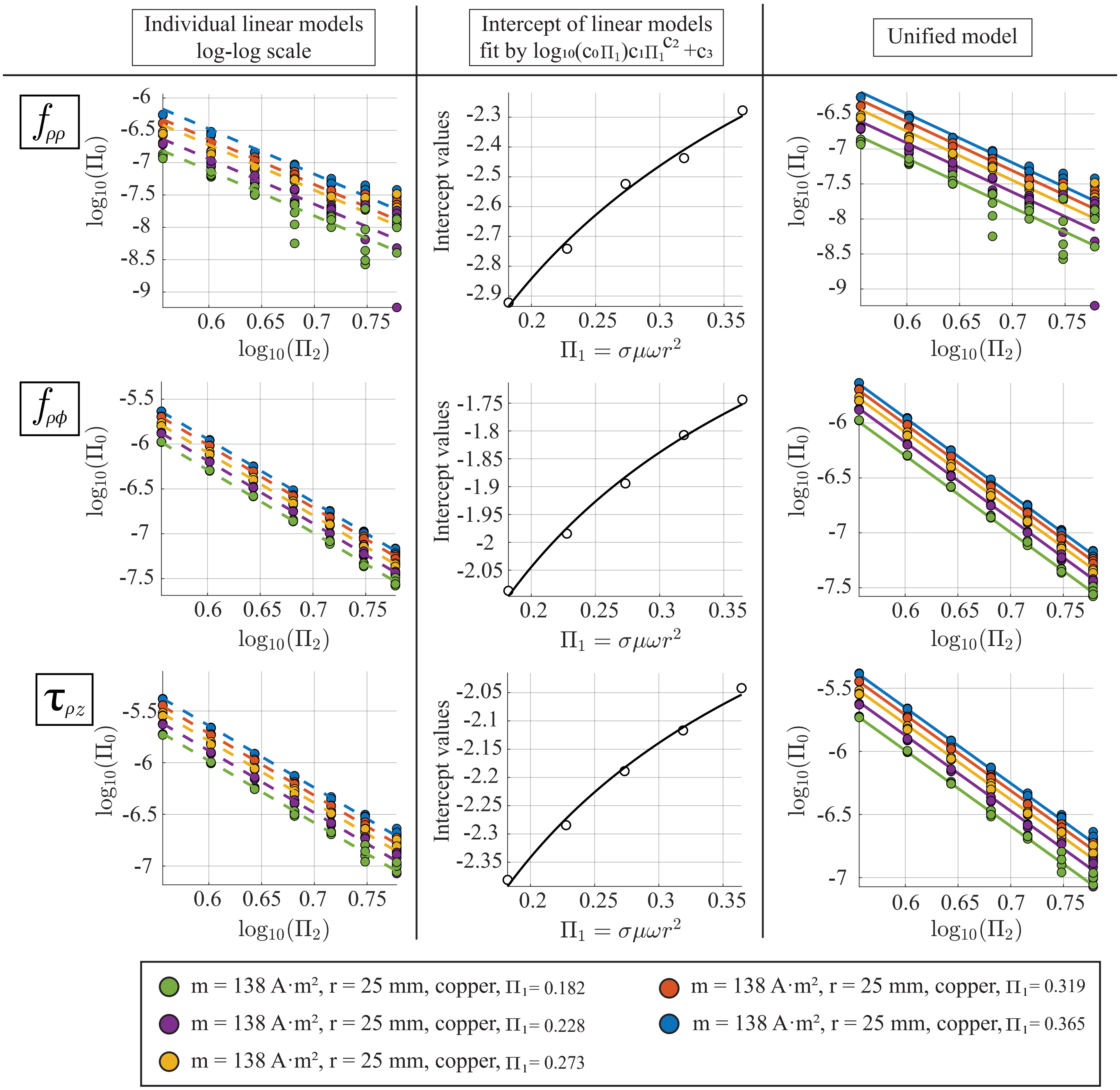

Figure S5: **Far-field model fitting for experimental results in the ρ configuration.** (Left) Linear models are fit to $\log_{10}(\Pi_0)$ vs. $\log_{10}(\Pi_2)$ for individual Π_1 values, with a slope of -7 for forces and -6 for torques. For clarity, only the lowest ω value from each set of m, r, and σ are shown. (Center) The resulting intercept values are fit with the model $\log_{10}(c_0\Pi_1)c_1{\Pi_1}^{c_2} + c_3$, using the complete set of Π_1 values. (Right) The final unified far-field model projected on the original data.

5 Comparison of Numerical and Experimental Results

Figure S6 shows a comparison of four items: (1) the experimental data, as described in Supplementary Information 4; (2) the model fit to the experimental data, as described in Supplementary Information 4; (3) the model fit to the FEA data set from Supplementary Information 2, as described in Supplementary Information 3; and (4) new FEA data at the same Π_1 and Π_2 values of the experimental data, which were not part of the model's training set, although they still fall within the range of Π_1 and Π_2 values used to fit the model. The experimental data points and experimental-based model are in good agreement with each other. The FEA-based model shows agreement with the new FEA data for the ρ configuration, and overpredicts the new FEA data for the z-axis configurations. Such variances between individual data and the model is not unexpected, given the wide range of Π_1 and Π_2 values used for model fitting, as well as the variance in Π_0 observed in Figs. S2 and S3. This variance will result in the FEA-based model over- and under-predicting FEA data for different system configurations. When comparing the FEA-based model and experiment-based models across all configurations and force-torque components, we see that the FEA-based model tends to over predict the experimental values of Π_0 by a factor of 1.5–5.5. We also see that the FEA data tends to overpredict the experimental data in this experimental range, but by a lesser extent in the z-axis configurations.

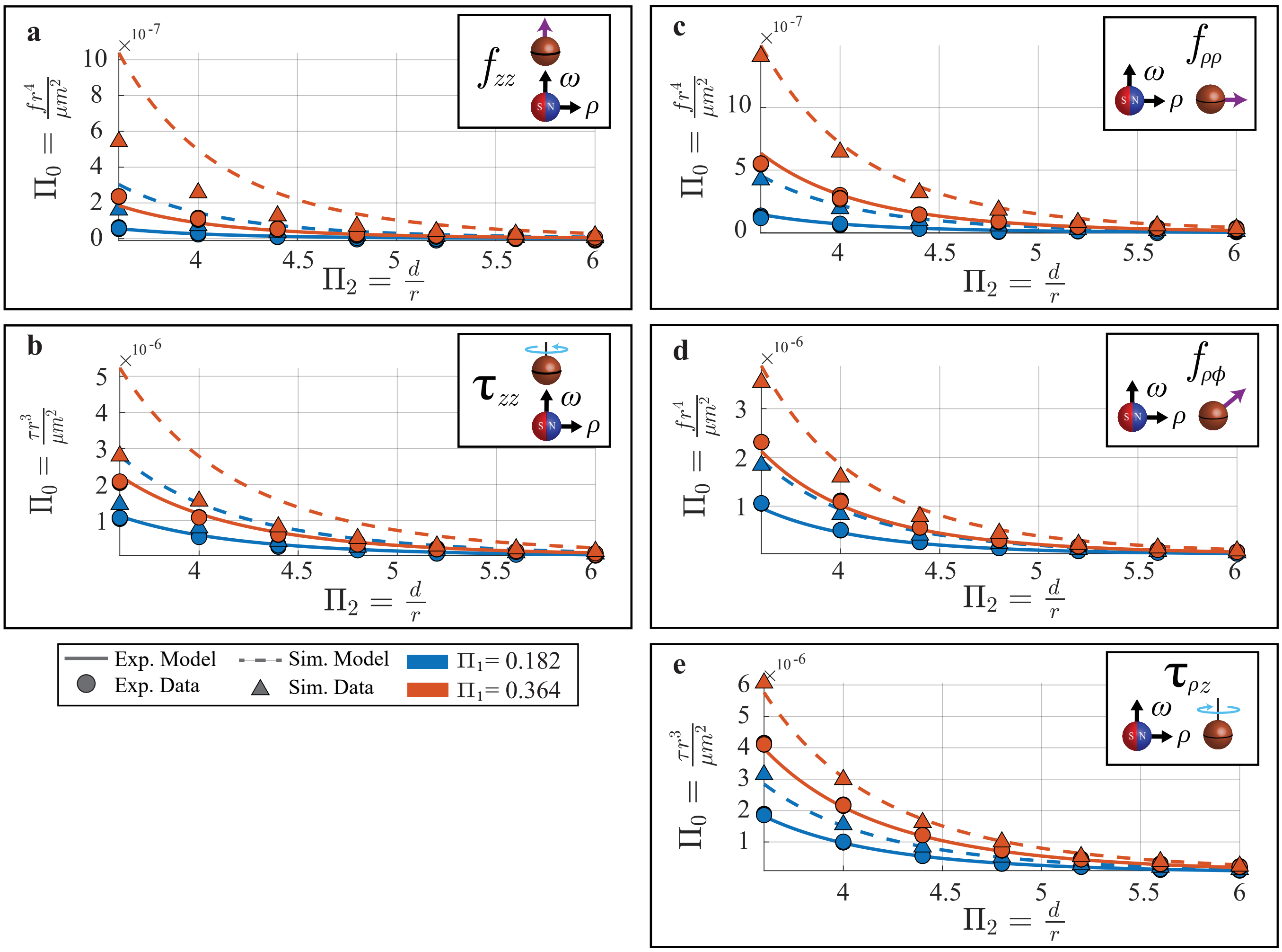

Figure S6: **Experimental results for all force and torque characterization with subset of experimental data, experiment-based models, FEA-based models, and new FEA data not included in the training set.** For clarity only a subset of experimental data is shown (minimum and maximum frequencies tested, corresponding to $\Pi_1 = 0.182$ and $\Pi_1 = 0.364$, respectively). **a**, z-axis configuration, f_{zz}. **b**, z-axis configuration, τ_{zz}. **c**, ρ configuration, $f_{\rho\rho}$. **d**, ρ configuration, $f_{\rho\phi}$. **e**, ρ configuration, $\tau_{\rho z}$.

6 Manipulation Numerical Simulations

We constructed a computer-simulated environment to run 3D-pose (i.e., 6-DOF) object-manipulation experiments. This simulator enabled us to simulate an environment without gravity and gives the added benefit of letting us observe the state directly. We chose a somewhat-arbitrary sampling rate of 1 Hz based on the system's relatively slow velocities and accelerations, so we can assume the object is relatively stationary with respect to the magnets over this time interval. Recall that our force-torque model was developed with stationary objects. We use standard rigid-body object dynamics to simulate the motion of the conductive object at 500 Hz (representing continuous-time, approximately) [3, 4]. We define ${}^{c}\boldsymbol{V}$ and ${}^{c}\boldsymbol{\omega}$ as the velocity and angular velocity, respectively, of the object with respect to the world frame, expressed in the conductive-object frame. We denote the skew-symmetric cross-product matrix derived from vector $\boldsymbol{v}$ as $\boldsymbol{v}^{\times}$ (such that for two vectors $\boldsymbol{v}_1$ and $\boldsymbol{v}_2$, $\boldsymbol{v}_1^{\times}\boldsymbol{v}_2 = \boldsymbol{v}_1 \times \boldsymbol{v}_2$). We denote the combined moment of inertia and mass matrix as $\boldsymbol{\mathcal{I}}$; in our case of a spherical object this reduces to a diagonal matrix, but the equations below and our approach hold for the general case.

We now develop the continuous-time dynamic equations. The conductive object's 6-DOF pose is represented by the transformation matrix ${}^{w}\boldsymbol{T}_c$. The time derivative of the object's pose is described by

$$ {}^{w}\dot{\boldsymbol{T}}_c = {}^{w}\boldsymbol{T}_c \begin{bmatrix} {}^{c}\boldsymbol{\omega}^{\times} & {}^{c}\boldsymbol{V} \\ \boldsymbol{0} & 0 \end{bmatrix} \tag{S5} $$

The continuous-time dynamics are governed by

$$ \begin{bmatrix} {}^{c}\dot{\boldsymbol{\omega}} \\ {}^{c}\dot{\boldsymbol{V}} \end{bmatrix} = \boldsymbol{\mathcal{I}}^{-1} \begin{bmatrix} -{}^{c}\boldsymbol{\omega}^{\times} & -{}^{c}\boldsymbol{V}^{\times} \\ \boldsymbol{0} & -{}^{c}\boldsymbol{\omega}^{\times} \end{bmatrix} \boldsymbol{\mathcal{I}} \begin{bmatrix} {}^{c}\boldsymbol{\omega} \\ {}^{c}\boldsymbol{V} \end{bmatrix} + \boldsymbol{\mathcal{I}}^{-1} \begin{bmatrix} {}^{c}\boldsymbol{\tau} \\ {}^{c}\boldsymbol{f} \end{bmatrix} \tag{S6} $$

This can be interpreted as the object's acceleration due to the gyroscopic and Coriolis forces summed with the object's acceleration due to external forces and torques acting on the object (i.e., our magnetic control input).

In order to numerically integrate these continuous-time dynamics, we must approximate them with the associated discrete-time equations for a small time-step dt. In the following equations we use ${}^{c}\boldsymbol{V}[t]$ to index

$\boldsymbol{V}$ at time t written with respect to the conductive-object frame.

$$ {}^{w}\boldsymbol{T}_c[t+dt] = {}^{w}\boldsymbol{T}_c[t] + {}^{w}\dot{\boldsymbol{T}}_c[t]dt \tag{S7} $$

$$ \begin{bmatrix} {}^{c}\boldsymbol{\omega} \\ {}^{c}\boldsymbol{V} \end{bmatrix} [t+dt] = \begin{bmatrix} {}^{c}\boldsymbol{\omega} \\ {}^{c}\boldsymbol{V} \end{bmatrix} [t] + \begin{bmatrix} {}^{c}\dot{\boldsymbol{\omega}} \\ {}^{c}\dot{\boldsymbol{V}} \end{bmatrix} [t]dt \tag{S8} $$

where the input accelerations are computed from Eq. S6.

We constructed our trajectories by specifying a series of waypoint poses and associated target times to reach each waypoint. These points were then used to build time-parameterized cubic polynomials between the waypoints as a target trajectory. The waypoint poses were given as positions and Euler angles so we can construct six independent polynomials. The desired positions and Euler angles were then converted to a desired transformation matrix for use in our controller. Formally, the cubic polynomials are defined as

$$ \begin{bmatrix} \boldsymbol{x} \\ \dot{\boldsymbol{x}} \end{bmatrix} [t] = \begin{bmatrix} \boldsymbol{p}_3 t^3 + \boldsymbol{p}_2 t^2 + \boldsymbol{p}_1 t + \boldsymbol{p}_0 \\ 3\boldsymbol{p}_3 t^2 + 2\boldsymbol{p}_2 t + \boldsymbol{p}_1 \end{bmatrix} \tag{S9} $$

where $\boldsymbol{p}_3$, $\boldsymbol{p}_2$, $\boldsymbol{p}_1$, and $\boldsymbol{p}_0$ are column vectors of length six representing the 3D pose of the conductive object. The constructed trajectory contains desired transformation matrices and velocity targets for each timestep.

We tuned a proportional-derivative (PD) controller to produce the error-based forces and torques to track the desired trajectory in the simulation. Orientation errors were computed as the minimum rotation between current and desired orientations using the axis-angle representation. The PD controller produced the desired forces and torques to feed into our optimization from Eq. 4equation.0.4. We tuned the control gains to operate well in both the numerical simulations and the physical experiments described in Supplemental Information 7. The proportional gains were 5×10^{-3} N/m and 1×10^{-5} N·m/rad for position and angle, respectively, and the derivative gains were 5×10^{-3} N·s/m and 1×10^{-5} N·m·s/rad for velocity and angular velocity, respectively.

Given a desired force-torque wrench, we leveraged our eddy-current-induced force-torque model and attempted to match the desired wrench as closely as possible, which we formalize in Eq. 4equation.0.4. We rotated the magnetic dipole at $\omega = 15$ Hz in all simulations. Our force-torque model supports a single electromagnet dipole source actuating in one of three discrete actions. Thus, to solve this optimization, we instantiated a separate continuous optimization problem for each discrete electromagnet-action combination. For each such combination, we used the Adam optimizer [5] (although other solvers would also work) to find the best combination of continuous decision variables to minimize the weighted squared error between desired and achievable force-torque.

Given our decision to use an unconstrained optimizer, we created box constraints on each bounded control variable α using the continuously differentiable sigmoid function

$$\alpha(\beta) = \frac{\alpha_{\max} - \alpha_{\min}}{1 + e^{-\beta}} + \alpha_{\min} \tag{S10}$$

where β can take on any real number. For $\alpha = m$, we use $\alpha_{\min} = 0$ and $\alpha_{\max} = m_{\max} = 40\,\mathrm{A{\cdot}m^2}$. For $\alpha = \theta$, we use $\alpha_{\min} = -\pi$ rad and $\alpha_{\max} = \pi$ rad.

To select the best discrete choice, we take the argument that minimizes the results over all of the independent continuous optimizations associated with the $3n$ possible electromagnet-action combinations.

The weighting, encoded by $\boldsymbol{Q}$, between different degrees of freedom in our cost function can be used to tune the optimization to prioritize specific dimensions. This weighting captures the units' various scaling, the inertia in various axes resisting motion, the difference in scale between different waypoint dimensions, and the aggressiveness of the controller in different dimensions. We found that a weight of 1 in all force dimensions and a weight of 200 in all torque dimensions (with all off-diagonal elements set to 0) resulted in a reasonable (although somewhat arbitrary) balance between position and orientation error.

The results of a typical 6-DOF manipulation simulation is shown in Figs. 3a–3d, as well as Supplemental Videos 1 and 2. In this simulation, the initial position of the conductive sphere is aligned with the origin, and is commanded to move first to one corner of a cube and then along the edges of that cube, displaying controlled motion in each direction. The target time to reach each waypoint was set to 5 minutes of simulated time, which we found to provide a reasonable trade-off between completion time and performance, although we make no claims of optimality. Over many trials, we found that the performance was fairly insensitive to the start and goal poses, provided they were sufficiently surrounded by the magnetic-dipole sources and given an adequate amount of time. Simulations were conducted first with 3-DOF position control in which orientation was uncontrolled (with object tumbling resulting), and then with full 6-DOF pose control with orientation controlled to maintain a fixed orientation. The exact waypoints for the simulations are provided in Table S5.

Time (s)	x (mm)	y (mm)	z (mm)
300	75	-75	-75
600	-75	-75	-75
900	-75	75	-75
1200	75	75	-75
1500	75	75	75
1800	-75	75	75
2100	-75	-75	75
2400	75	-75	75
2700	75	-75	-75

Table S5: **Waypoints from manipulation simulations.** The waypoints are used with Eq. S9 to construct trajectories used for manipulation simulations.

7 Manipulation Experiments

Accurate Earth-based microgravity simulation is challenging. The characteristics of a true microgravity simulation are that it enable 6-DOF motion, that it be gravity-free or gravity-compensated, and that it be drag-free. A variety of Earth-based test environments are commonly used [6, 7]: the KC-135 "vomit comet" reduced-gravity aircraft; an air-bearing test facility; passive and active manipulator and gimbal combinations to counter gravity; and neutral buoyancy (e.g., a water tank). Each of these techniques has drawbacks. KC-135 provides a true microgravity simulation, but its cost and availability make its use prohibitive for academic research, and its short duration (20–30 s) make it of limited use for experiments with long time scales. Air-bearing test facilities only enable 3-DOF mobility in a horizontal plane (i.e., 2-DOF position, 1-DOF orientation). Both passive and active gravity compensation implicitly assume that the forces and torques being intentionally generated on the object are large compared to any unmodeled forces and torques and/or force-torque sensor noise. Neutral buoyancy in water adds significant drag that would not be present in space.

For our manipulation experiments, we chose to use a raft floating on the surface of water (see Fig. 3e). This solution is effectively a hybrid of the air-bearing technique and the neutral-buoyancy technique, and inherits the limitations of both. The tank of water was suspended above four identical omnidirectional electromagnets referred to as Omnimagnets, which have been previously described [8], as the dipole sources. Each Omnimagnet comprises three mutually orthogonal nested coils with a spherical ferromagnetic core in the center, and was designed such that its field could be accurately modeled by the point-dipole equation even at relatively close distances. The coils were connected to individual current-drive amplifiers (AMC16A8, Advanced Motion Control), with current and voltage limits of 8 A and 80 V, respectively. All of the amplifiers were connected in a parallel configuration to one power supply (PS16L80, Advanced Motion Control) with current and voltage limits of 10 A and 80 V, respectively. This limits the maximum dipole strength that can be achieved in every direction to $40\,\mathrm{A{\cdot}m^2}$. The dipole's strength and rotation frequency both have a direct relation to the induced force and torque. The dipole strength is linearly related to the current in the coils. Each coil's inductance limits how rapidly the current can be changed, and therefore limits the maximum frequency of the dipole rotation for a given dipole strength. We found this maximum frequency empirically by mounting a 25-mm-radius copper sphere on an ATI Nano17 Titanium force-torque sensor and collecting data at two representative locations near an Omnimagnet. Using the maximum dipole strength of $40\,\mathrm{A{\cdot}m^2}$, frequencies between 1 Hz and 20 Hz were tested, with the peak force and torque observed at 15 Hz. Thus, we use a constant magnetic dipole rotation of $\omega = 15\,\mathrm{Hz}$ in all manipulation experiments.

To calculate the necessary current to generate the required dipole, we used the linear approximation [9]:

$$\boldsymbol{m} = \alpha \mathbf{I} \tag{S11}$$

where $\boldsymbol{m}$ is the dipole moment (units $\mathrm{A{\cdot}m^2}$), $\boldsymbol{I}$ is the column vector of the corresponding coil currents (units A), and $\alpha = 7.00\,\mathrm{m^2}$ is a coefficient that was found via calibration by recording magnetic-field measurements well beyond the minimum bounding sphere of the Omnimagnet and fitting the data to the point-dipole model of Eq. 1equation.0.1.

The centers of the Omnimagnets were placed on the corners of a 200 mm square in a horizontal plane, fixed using a 3D-printed jig. A camera (Grasshopper3, FLIR) operating at 20 Hz was rigidly mounted centered above the tank. A 20-mm-radius copper sphere was placed in the center of a 3D-printed cylindrical flat-bottom raft, which floated on the surface of the water, such that the center of the copper sphere was 150 mm above the plane of the Omnimagnets. An ArUco marker used for camera-based tracking was placed on top of the raft [10], which enabled pose estimates at 20 Hz. A univariate spline in each DOF was fit to the 1000 most recent pose detections (i.e., the past 50 s) [11], and these splines were used to get smoothed velocity estimates.

Five trials were performed for each of the two distinct experiments. In both experiments, the raft (i.e., the copper sphere) was commanded to move along a 150 mm square with 2-DOF position control. In one experiment, the orientation was not controlled, with the raft being allowed to freely rotate about the vertical axis. In the other experiment, the rotation about the vertical axis was also controlled, for a total of 3-DOF control over the raft's pose. The surface of the water resisted motion in the remaining 3-DOF. The PD controller gains used were the same as those used in the numerical manipulation simulations of Supplementary Information 6. The exact waypoints for the physical experiments are provided in Table S6. The method to convert the waypoints to a full trajectory is the same as described in Supplementary Information 6. The $\boldsymbol{Q}$ matrix used in the optimization was the same used in the numerical simulations of Supplementary Information 6, but we also set uncontrolled dimensions to zero. For 2-DOF position control,

Time (s)	x (mm)	y (mm)	angle (rad)
2-DOF Position Control			
240	75	75	NA
480	-75	75	NA
720	-75	-75	NA
960	75	-75	NA
1200	75	75	NA
3-DOF Pose Control			
240	75	75	$\frac{\pi}{4}$
480	75	75	π
720	-75	75	π
960	-75	75	$\frac{3\pi}{2}$
1200	-75	-75	$\frac{3\pi}{2}$
1440	-75	-75	2π
1680	75	-75	2π
1920	75	-75	$\frac{5\pi}{2}$
2160	75	75	$\frac{5\pi}{2}$
2400	75	75	3π

Table S6: **Waypoints from manipulation experiments.** The waypoints are used with Eq. S9 to construct trajectories for manipulation experiments.

$Q = \texttt{diag}(1, 1, 0, 0, 0, 0)$, and for 3-DOF pose control, $Q = \texttt{diag}(1, 1, 0, 0, 0, 200)$, where $\texttt{diag}(i, j, ...)$ is the square diagonal matrix with $i, j, ...$ as its ordered diagonal elements. Figure S7 shows the complete trajectory results for these experiments. One representative trial from each experiment was presented in Figs. 3f and 3g; in Fig. S8 we provide the complete position and orientation results as a function of time for these trials.

The trajectory-following accuracy and precision across the five trials in each experiment are quantitatively summarized in Fig. S9. To quantify the accuracy at each time t, we compute the position and velocity errors using the 2-norm, and we compute the magnitudes of the orientation and angular-velocity errors. These combined results across time can be seen in Fig. S9. To quantify the precision (i.e., repeatability across trials) of each experiment, we first take the covariance of the x–y position across all trials at each time t. These covariances can be seen in Fig. S7 where we draw a 95% confidence ellipse at each time t, computed using the principal components of each covariance matrix. In addition, we take the determinant of these covariance matrices to get the generalized positional variance at each time t; to get this generalized positional variance back to the original measurement unit of interest, we take the square root. These values can then be treated as a scalar measure of precision over time. We similarly compute the square root of

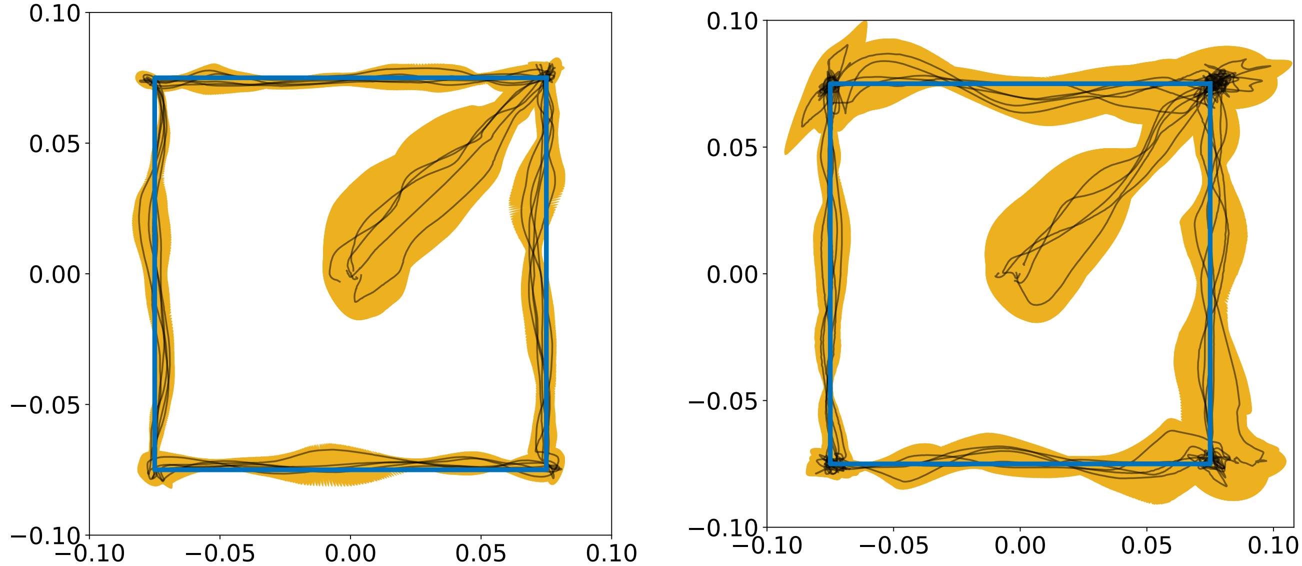

2-DOF Position Control

3-DOF Pose Control

Figure S7: **Position trajectories across five trials of each manipulation experiment.** The blue square is the desired trajectory and black curves show the actual trajectories for individual trials. The yellow shaded region depicts 95% confidence ellipse.

generalized velocity variance. Because orientation and angular velocity are both 1-DOF variables in our experiment, we can directly utilize the standard deviations of orientation and angular velocity at each time t. These combined results across time can be seen in Fig. S9.

In the future, neutral buoyancy seems to be the most promising technique to transition manipulation experiments to full 6-DOF.

It would require that we create a neutrally-buoyant object fully enclosing a conductive object at its center. This would be challenging, but not impossible. Any imperfection in the neutral buoyancy would need to be significantly less than the magnitude of the eddy-current-induced forces generated on the conductive object. If we imagine an air-filled bubble-like structure with a copper sphere of radius r at its center, the bubble-like structure would need to have a radius of approximately $2.1r$. For an aluminum sphere, this value would need to be approximately $1.4r$. The dipole-field sources themselves would not need to be submerged in water. Object tracking would similarly become more challenging requiring multiple markers/cameras to account for occlusions.

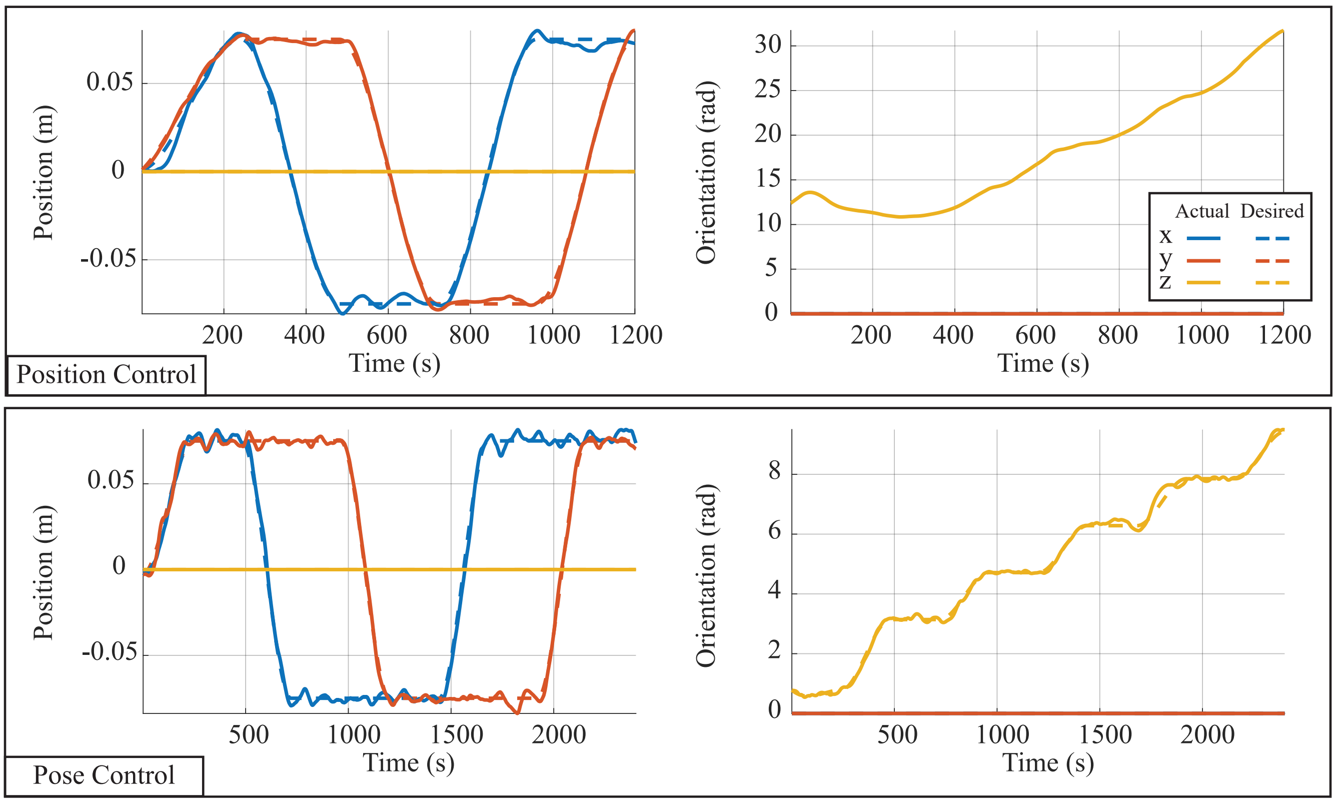

Figure S8: **Position and orientation values versus time for the 2-DOF position-control experiment and 3-DOF pose-control experiments shown in Figs. 3f and 3g, respectively**. The z axis represents the vertical axis.

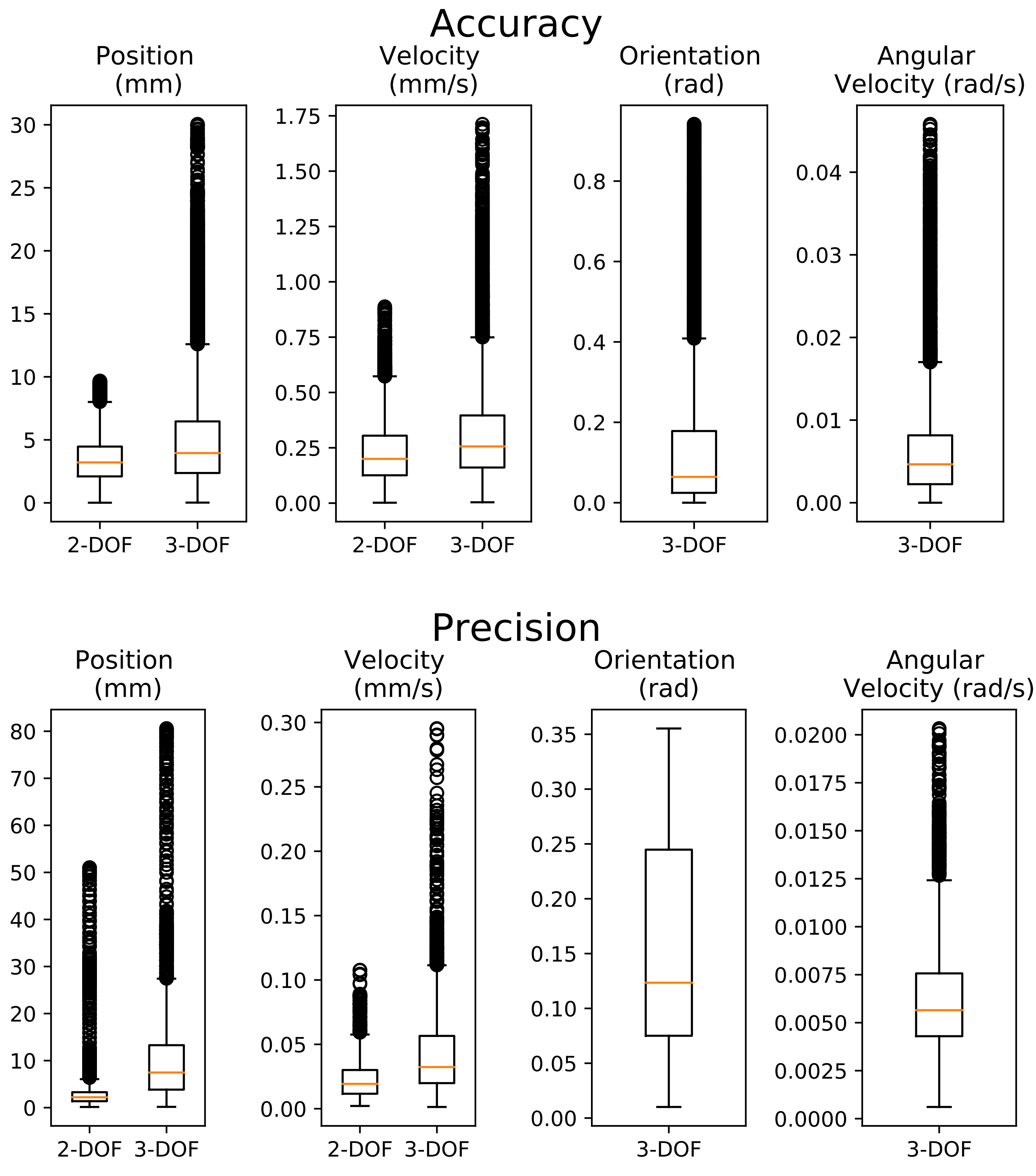

Figure S9: **Quantitative results across five trials of each manipulation experiment.** "2-DOF" refers to the position-control experiment (in which orientation was uncontrolled) and "3-DOF" refers to the pose-control experiment. Definition of box-plot elements: red center line, median; box limits, upper and lower quartiles; whiskers, 1.5× interquartile range; circles, outliers.

8 Discussion

It is worth noting that the force components that tend to push the conductive sphere away from the rotating dipole increase asymptotically (i.e., with diminishing return) with an increase in Π_1 (e.g., an increase in ω), at least over the range of Π_1 values considered here; see column 2 of Figs. S2 and S3. This would suggest an actuation policy that is to spin the magnetic dipole as fast as possible. However, the other force component and both torque components increase to a maximum value at relatively low value of Π_1, and then decrease with further increases in Π_1. This would suggest that distinct optimal dipole rotation frequencies exist to generate each of those components.

However, it may also be possible to find a dipole rotation frequency that is near optimal for all force-torque components. Considering all five force-torque components holistically, it would seem that designing a system to achieve $1 \leq \Pi_1 \leq 5$ (i.e., $\Pi_1 \approx 3$, with results insensitive to small changes in Π_1 around this value) may be close to optimal. If we consider the form of Π_1, it would suggest a near-optimal dipole rotation frequency for a given piece of conductive material of the form

$$\omega \approx \frac{3}{\sigma \mu_0 r^2}\,\text{Hz} \tag{S12}$$

It is interesting to note that this value depends on the conductivity and size of the object, but not on the distance or strength of the dipole-field source.

In the manipulation experiments of Fig. 3, we manipulated a copper sphere ($\sigma = 5.8 \times 10^7$ S/m) with a radius $r = 0.020\,\text{m}$. This would suggest a near-optimal rotation frequency would have been 103 Hz. This value does not account for the practical amplifier and power-supply limitations of our field-generation system (since the magnitude of the dipole strength, m, appears in Π_0). In our manipulation experiments, we used a value of $\omega = 15\,\text{Hz}$, which corresponds to $\Pi_1 = 0.44$.

There are estimated to be 34,000 objects in orbit greater than 10 cm, 900,000 objects less than 10 cm and greater than 1 cm, and 128 million objects less than 1 cm and greater than 1 mm [12]. Let us consider pieces of aluminum (approximated as spheres, with $\sigma = 3.8 \times 10^7$ S/m), since aluminum is the most common material found in space debris [13]. Equation S12 enables us to determine the near-optimal dipole rotation frequency as a function of the size of the object, which is depicted in Fig. S10 for the range of sizes that are prevalent in space debris. For reference, brushless DC motors with speeds as high as

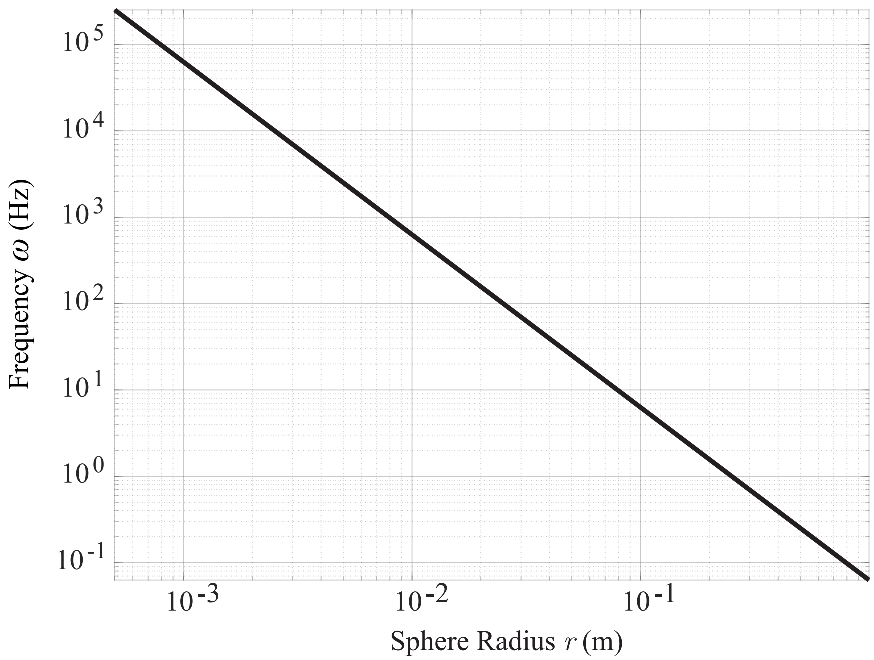

Figure S10: **Near-optimal frequency of magnetic-dipole rotation vs. aluminum-sphere radius.**

120,000 rpm (2,000 Hz) can be purchased from Maxon, although there would be practical challenges in spinning a magnet so rapidly.

Using these optimal values, we can approximate the forces and the resulting accelerations that can be imparted on aluminum pieces of various sizes by calculating the ratio of the eddy-current-induced forces to the mass of the object (using a density of 2,710 kg/m^3). Let us consider the same cubic NdFeB permanent magnet used in our experiments, which has a side length of 51 mm and magnetic dipole strength of $m = 138\,\mathrm{A{\cdot}m^2}$, as our dipole-field source. Such a magnet could be positioned and rotated by a robotic manipulator. Of course, it is easy to conceive of larger/stronger dipole-field sources, but since m effects force quadratically and m is linear with respect to the magnet's volume, it will be easy to extrapolate these results to a magnet of a different size via a magnet volume ratio. When the cubic magnet rotates rapidly about arbitrary axes, it will conservatively sweep out a volume equal to its minimum bounding sphere, which has a radius of $\sqrt{0.75(51)^2} = 44$ mm. For a given piece of aluminum, we are only interested in permanent-magnet positions in which the magnet's minimum bounding sphere does not collide with the aluminum object. If this includes position for which $\Pi_2 < 1.5$, we should expect the results to be conservative (i.e., underpredict the actual forces). In Fig. S11, we show the expected Π_0 values, forces, and accelerations for each of the non-zero force components for three different sizes (i.e., diameters) of aluminum sphere (called out in [12] and discussed above) as a function of the distance between the surface of the aluminum sphere

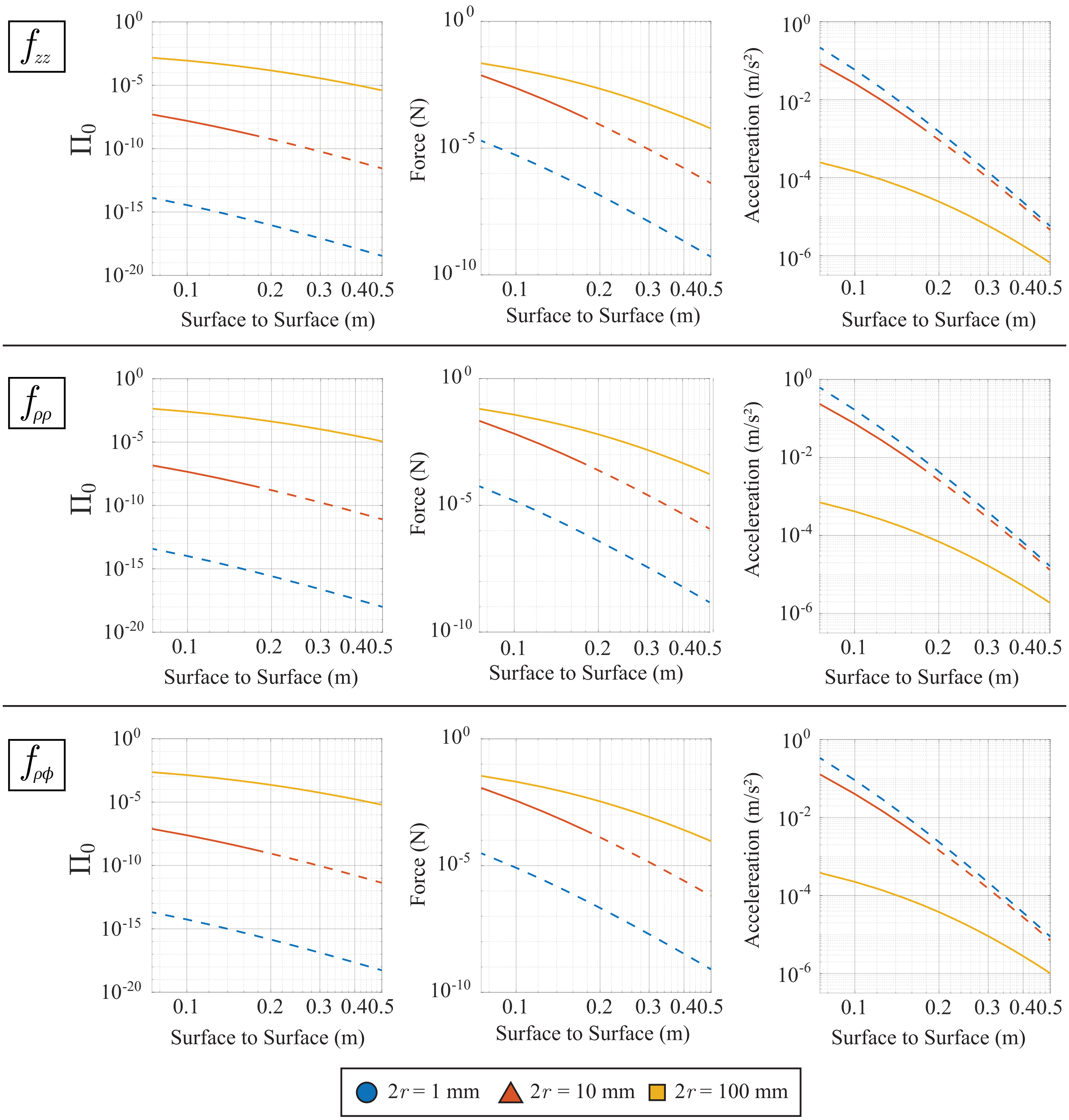

Figure S11: **Near-optimal forcing in each canonical direction—provided as Π_0, force, and acceleration—as a function of the surface-to-surface distance between the aluminum sphere and the minimum bounding sphere of the rotating cubic permanent magnet, for three different aluminum spheres.** Portions of the curves with dashed lines are extrapolations beyond the Π_2 values used to develop our model.

and the surface of the cubic magnet's minimum bounding sphere (i.e., $d - r - 0.044\,\mathrm{m}$), using the ω values from Fig. S10.

9 References

[1] Abbott, J. J., Diller, E., & Petruska, A. J. Magnetic methods in robotics. *Annu. Rev. Control Robot. Auton. Syst.* **3**, 57–90 (2020).

[2] Mirica, K. A., Ilievski, F., Ellerbee, A. K., Shevkoplyas, S. S. & Whitesides, G. M. Using magnetic levitation for three dimensional self-assembly. *Adv. Mater.* **23**, 4134–4140 (2011)

[3] Lynch, K. M., & Park, F. C. Modern robotics: mechanics, planning, and control. (Cambridge University Press, Cambridge, UK, 2017)

[4] Jiang, L., Wang, Y. & Xu, S. Integrated 6-dof orbit-attitude dynamical modeling and control using geometric mechanics. *Int. J. Aerosp. Eng.* 4034328 (2017)

[5] Kingma, D. P. & Ba, J. Adam: a method for stochastic optimization. *arXiv preprint arXiv:1412.6980* (2014)

[6] Atkins, E. M., Lennon, J. A., & Peasco, R. S. Vision-based following for cooperative astronaut-robot operations. *IEEE Aerosp. Conf.* 215–224 (2002)

[7] Memon, C., Busolo, S., Cocuzza, S., Aboudan, A., Bulgarelli, A., Bettanini, C., Marchesi, M., & Angrilli, F. Issues and solutions for testing free-flying robots. *Acta Astronaut.* **60**, 957–965 (2007)

[8] Petruska, A. J., Brink, J. B., & Abbott, J. J. First demonstration of a modular and reconfigurable magnetic-manipulation system. *IEEE Int. Conf. on Robotics and Automation* 149–155 (2015)

[9] Petruska, A. J., & Abbott, J. J. Omnimagnet: an omnidirectional electromagnet for controlled dipole-field generation. *IEEE Trans. Magn.* **50**, 8400410 (2014)

[10] Garrido-Jurado, S., Muñoz-Salinas, R., Madrid-Cuevas, F., & Marín-Jiménez, M. Automatic generation and detection of highly reliable fiducial markers under occlusion. *Pattern Recognit.* **47**, 2280–2292 (2014)

[11] Virtanen et al. SciPy 1.0: fundamental algorithms for scientific computing in python. *Nat. Methods* **17**, 261–272 (2020)

[12] The European Space Agency. Space debris by the numbers. https://www.esa.int/Safety_Security/Space_Debris/Space_debris_by_the_numbers. Accessed: June 18, 2021. Information last updated on May 20, 2021.

[13] Opiela, J. N. A study of the material density distribution of space debris. *Adv. Space Res.* **43**, 1058–1064 (2009)